SANDIA REPORT

SAND98–1694
Unlimited Release
Printed July 1998

Statistical Cloud Coverage as a Function of Cloud Optical Thickness

Keith L. Brower

Prepared by
Sandia National Laboratories
Albuquerque, New Mexico 87185 and Livermore, California 94550

Sandia is a multiprogram laboratory operated by Sandia Corporation, a Lockheed Martin Company, for the United States Department of Energy under Contract DE-AC04-94AL85000.

Sandia National Laboratories

Issued by Sandia National Laboratories, operated for the United States Department of Energy by Sandia Corporation.

Available to DOE and DOE contractors from
Office of Scientific and Technical Information
P.O. Box 62
Oak Ridge, TN 37831

Prices available from (615) 576-8401, FTS 626-8401

Available to the public from
National Technical Information Service
U.S. Department of Commerce
5285 Port Royal Rd
Springfield, VA 22161

NTIS price codes
Printed copy: A03
Microfiche copy: A01

SAND98-1694
Unlimited Release
Printed July 1998

Statistical Cloud Coverage as a function of Cloud Optical Thickness

Keith L. Brower
Mission Analysis and Simulation
Sandia National Laboratories
P. O. Box 5800
Albuquerque, New Mexico 87185-0977

Abstract

The time-averaged, daylight fractional statistical cloud coverages as a function of cloud optical thickness and selected values of cloud transmission were determined for various geographic areas using D1 data from the International Satellite Cloud Climatology Project (ISCCP). The regions of interest chosen for this report are: global earth, global sea, global land, global coast, and the six 30° -latitude bands over sea, over land, and over coast with longitude $0° - 360°$.

Keywords: clouds, ISCCP, satellite.

Acknowledgments

Appreciation is expressed to Stephen Gentry and Raymond Ostensen for their review of this report and their suggestions and to Ellan Anderson and Martin Arrambide for technical assistance. The ISCCP D1 data used in this study were obtained from the NASA Langley Research Center EOSDIS Distributed Active Archive Center. This work was performed at Sandia National Laboratories and supported by the U.S. Department of Energy under Contract No. DE-AC04-94AL85000.

TABLE OF CONTENTS

THIS PAGE LEFT INTENTIONALLY BLANK.

LIST OF FIGURES

1 Introduction

This report presents cloud coverage statistics for various geographic regions as a function of cloud optical thickness. This statistical information is deduced from data determined from satellite measurements of terrestrial, atmospheric and cloud properties by the International Satellite Cloud Climatology Project (ISCCP) [1]. In particular our results are based on the ISCCP D1 data base, which is briefly described in Sec. 2. The technical definitions of the specific cloud statistics reported here are given in Sec. 3, and the results of our analysis are presented graphically in Sec. 4. This information is useful for assessing the statistical capabilities of satellite-based optical sensors with regard to imaging and detecting optical signals beneath clouds.

2 Description of the ISCCP D1 Data Base

The ISCCP B3 radiance database evolves from the analysis of satellite radiometric data [2, Fig. 1.2, p. 3]. "The original radiance data represent measurements over fields-of-view (FOV) ranging from 4 to 7 km in size at nadir (pixels); however, the Stage B3 data are sampled to a spacing of about 25 - 30 km. Although navigation accuracy may be higher for some satellites, overall accuracy is confirmed to be about ±25 km. The analysis to determine clear radiances uses the sampled data mapped to 25 km resolution; hence, we consider the smaller individual image pixels to represent a *sample* of the distribution of surface and cloud conditions over this larger spatial scale. Although the variability of surfaces and clouds is generally smaller at such small scales than at scales greater than approximately 100 km (Seze and Rossow [3, 4]), all pixel-level quantities are treated as having a certain amount of intrinsic variation about an average value representing the spatial domain of approximately 25 km in size. In any case, the cloud detection tests and radiative analysis are applied to the original image pixels, so we will continue to refer to the smallest unit of data as a pixel, whether it is the original image [4 - 7 km] pixel or the small 25 km domains from the mapped images." [5, p. 58]

The ISCCP DX database is derived from the satellite B3 radiance data together with the TV and IS datasets [5, p. 55]. The physical values contained within the DX database are assigned to surface map pixels measuring about 30 km [5, Fig. 3.4, p. 55] with a time resolution of 3 hours.

Each ISCCP D1 data file contains global atmospheric cloud data for one day. The time resolution of this data is 3 hours, and the spatial resolution is 280×280 km^2. For each of the eight 3-hour time slots and for each of the 6596 fixed equal-area ISCCP grid map cells measuring approximately 280×280 km^2, there are 202 data items. The values for various physical parameters within the D1 database are produced by merging and averaging 3-hour, 30-km pixel data from the DX database [5, p. 2, 43, 55]. Various physical quantities within the DX data base are based on satellite measurements over earth-pixel dimensions of 4 - 7 km having a location accuracy of approximately 30 km. At least 20 DX-pixel sample values that geographically overlap a selected 280-km D1 cell are used to determine the mean value, standard deviation, etc. of the corresponding physical parameters within the D1 data set [5, p. 45].

The available data presently spans the years 1986 through 1994. This data is available at web sites *http://isccp.giss.nasa.gov/* and *http://eosweb.larc.nasa.gov/HPDOCS/* along with extensive user documentation, programs for the extraction of data from the data files, and references to numerous scientific studies related to the understanding and interpretation of the satellite data from which the D1 and other data sets are evolved.

The D-series is a revised and improved version of the C-series data. In particular, the D1-series reflects improved detection of cirrus clouds over land, polar detection of clouds over ice and snow surfaces, and improved detection of low clouds at high latitudes. Particularly relevant to this study is the extension of the range of cloud optical thicknesses from approximately 120 to 378. Other improvements are noted in the documentation [5, p. 2].

2.1 Selected D1 Data Items

The byte numbers of the physical items extracted from the D1 data base for the purposes of this study are summarized in Table 1. The complete list of items in the D1 data base is given in reference 5, p. 19. Items number 13, 93, 98, 100, and 105 in Table 1 are based in part on infrared (IR) measurements at 11 microns. Other radiance measurements are at 3.7 microns (near infrared, NIR) and 0.6 microns (visible, VIS) [5, Table 2.5.4, p. 36]. Examination of D1 data indicates that item 92 is the average of items 93, 94, and 95; and item 99 is the average of items 100, 101, and 102 where items 94 (101) are IR-only-cloud pixels and items 95 (102) are NIR-only-cloudy pixels. Only the IR D1 data include the mean and standard deviation; other D1 data consist of only mean values. Unless stated otherwise, the various graphs presented in this report are based on our analysis of the IR D1 data. A comparison between the IR cloudy data and the cloudy data is made in Sec. 4.

Table 1: Sample of items from the ISCCP D1 data base.

Byte Number (1 - 202)	Description
6 (Data record prefix)	Hour, UTC (00, 03, 06, ..., 21), Data Record Prefix The date is implicit in the file name.
1	latitude (equal-area and equal-angle)
2	longitude (equal-area)
6	day/night/land/sea/coast
11	total number of pixel measurements
12	number of cloudy pixels
13	number of IR cloudy pixels
92	mean tau (albedo) for cloudy pixels
93	mean tau (albedo) for IR cloudy pixels
98	sigma-tau (albedo) for IR cloudy pixels
99	mean tau (water path) for cloudy pixels
100	mean tau (water path) for IR cloudy pixels
105	sigma tau (water path) for IR cloudy pixels

2.2 Hour, Latitude, Longitude

Each 202-data set contains data for a specific date, implicit in the name of the D1 file, the nominal time (to within ±1.5 hours of the nominal UTC times 00, 03, ..., 21), the latitude and longitude of the center position of a 280 kilometer equal-area cell [5, p. 16].

2.3 Day, Night, Land, Sea, Coast

The integer in byte number 6 indicates, for example, a day-land or night-coast combination that characterizes that particular 202-data set. Because of the nature of the optical cloud measurements, cloud optical thickness values are restricted to local daylight hours [5, p. 20]. Parameters restricted to daylight values necessarily include 0.6 micron (VIS) measurement data [5, p. 45].

A cell is defined to be a land cell if it overlaps earth surface containing at least 65% land; a sea cell overlaps earth surface with less than 35% land; cells with between 35 and 65% land are defined to be coastal [5, p. 45]. The statistical results in this report are for daylight over sea, land and/or coast.

2.4 Cloud Coverage

The cloud coverage as defined in this paper is the ratio of the number of cloudy IR pixels (byte number 13) to the total number of pixels (byte number 11) [5, p. 45]. The determination of cloudy IR pixels begins with the analysis of the 4 - 7 km pixel B3 data [5, p. 62]. "Cloudy conditions are defined by those radiances that are sufficiently different from the clear values in any spectral channel" [5, p. 56, 59].

2.5 Cloud Optical Thickness

The ISCCP cloud models are based on two microphysical models: one for water droplet clouds and one for ice crystal clouds [5, p. 47]. The most basic physical characteristic of any cloud is its (columnar) water content. The second feature that characterizes the optical properties of a cloud is the dimensions of the water droplets or ice crystals. In the case of the liquid water droplet model, ISCCP characterizes all cloud water droplets by spheres having a size distribution described by a gamma distribution with an effective mean radius of 10 microns and an effect variance of 0.15 [5, p. 47]. Knowing the cloud water density and geometrical thickness, the cloud optical thickness can be calculated [6, p. 19, Eq. 11]. The cloud optical thickness is given by

$$\tau = \frac{A_{cloud}}{\langle d_{scatter} \rangle}. \tag{1}$$

where A_{cloud} is the geometrical thickness of the cloud and $\langle d_{scatter} \rangle$ is the mean photon scattering distance between cloud water droplets. In the ISCCP model, ice crystals are characterized as random fractal shapes (practically all natural ice crystals are hexagonal in shape [7, 8]) with a -2 power law size distribution from 20 to 50 microns giving an effective radius of 30 microns and an effective variance of 0.10 [5, p. 47]. In the case of the NASA cloud models, $\langle d_{scatter} \rangle$ ranges approximately from 15 to 110 meters depending upon the cloud type [6, p. 19].

Cloud optical thickness (also referred to as tau, τ or COT) is proportional to the geometrical thickness of a cloud. The cloud optical thickness unit length is the photon mean scattering distance for photons of wavelength 600 nanometers scattered by the cloud water particulates [5, p.

47]. At 600 nm atmospheric absorption is minimal so that the extinction coefficient is essentially equal to the scattering coefficient. This 600 nm wavelength is not be confused with the wavelengths of the radiance measurements, e. g. IR, NIR, VIS which determine cloud albedo or water content from which cloud optical thickness or tau values at 600 nm are determined [5, p. 47, 78]. Because half of the scattering cross section is due to strong forward scattering arising from diffraction by the water particulates [9, 107], one can "see through" thin clouds.

A cloud optical thickness value should be consistent with a cloud's albedo and its water content. The cloud optical thickness given by byte number 93 is consistent with the average cloud albedo. The albedo cloud optical thickness is obtained by averaging individual 30-kilometer pixel tau values with non-linear weights so as to preserve the average cloud albedo [5, p. 47]. The mean water path for cloudy pixels in byte number 100 is expressed in terms of the water path cloud optical thickness. The mean cloud water-path content is (approximately) equal to the cloud optical thickness (tau_wp, unitless number) times a constant of proportionality. For liquid water clouds, this constant is 6.292 grams/meter^2, and for ice clouds it is 10.500 grams/meter^2 [5, p. 47]. The water-path cloud optical thickness is determined by a linear average of pixel tau values [5, p. 47]. Statistics for both the tau water path (tau_wp) and the tau albedo (tau_a) are presented in Sec. 4.1 and Sec. 4.2, respectively.

Steve Gentry [10] and Ray Ostensen [11] have pointed out that a significant problem can arise in attempting to deduce the probability distribution of clouds as a function of cloud optical thickness from the ISCCP D1 database. Because the cloud optical thicknesses are the average of individual tau values associated with 4 - 7 km pixel measurements contained within a 280-km cell, there is significant variation in tau values that can be lost particularly for nonuniform clouds if only the mean tau values are considered. Gentry [10] suggested this information might be recovered statistically by taking into consideration the standard deviation associated with, for example, the mean cloudy IR tau value (see Table 1). These effects are taken into consideration in our statistical analysis (Sec. 3).

3 Cloud Statistics

3.1 Q Data Matrix

A 3-dimensional data matrix $Q_{i,j,k}$ is defined from which all of the cloud statistical distributions presented in this report are determined. The index i denotes a cell location, index j denotes a date and time, and index k denotes one of the 244 tau values (τ_k with discrete values 0.00, 0.02, 0.04, 0.06, 0.09, 0.11, 0.14, ..., 10.59, 10.78, 10.97, ..., 92.02, 96.40, 101.01, ..., 282.78, 323.92, 378.65) for this cell and time. We also know for any given cell location as specified by the value of i the dominant surface type (daylight-sea, etc.). The value assigned to $Q_{i,j,k}$ is defined to be

$$Q_{i,j,k} = \frac{W_{i,j,k} C_{i,j}}{243}, \qquad (2)$$

$$\Delta\tau_k \sum_{l=1} W_{i,j,l}$$

where

$$\Delta\tau_k = \tau_k - \tau_{k-1} \tag{3}$$

and τ_k is the upper cloud optical thickness for the kth bin. Division by $\Delta\tau_k$ makes $Q_{i,j,k}$ a differential distribution which can subsequently be integrated over τ. These values of τ_k are defined in the C and Fortran computer codes used to read the D1 data files. (The systematic fluctuations in the dashed curve in Figure 1, Figure 19, and Figure 20 are due to the truncation of τ_k to an accuracy of 0.01 in these computer codes.) That fraction of the geographic cell i at time j, $C_{i,j}$, that is covered by clouds is defined by us to be

$$C_{i,j} = \frac{[NumberCloudy(IR)Pixels]_{i,j}}{[TotalNumberPixels]_{i,j}} \; . \tag{4}$$

The terms in the numerator and denominator are given in the D1 database (Table 1). The parameter $W_{i,j,k}$ is a weighting factor. For example, if $Q_{i,j,k}$ were based on only the mean cloud optical thickness values, then $W_{i,j,k}$ would be equal to 1 if $\tau_{k-1} < \tau_{mean} \leq \tau_k$ else W_k would be equal to 0; this approach applies only to uniform cloud coverage. In order to account for variations in cloud optical thickness within the 280-km cell, we assume that the distribution in cloud optical thicknesses can be represented statistically by a gaussian distribution

$$W_{i,j,k} = \frac{1}{2}\left[erf\left(\frac{\tau_k - \tau_{i,j}^{mean}}{\tau_{i,j}^{sigma}\sqrt{2}}\right) - erf\left(\frac{\tau_{k-1} - \tau_{i,j}^{mean}}{\tau_{i,j}^{sigma}\sqrt{2}}\right)\right] \; . \tag{5}$$

$\tau_{i,j}^{sigma}$ is the standard deviation in cloud optical thickness associated with cell i at time j and is given by

$$\tau_{i,j}^{sigma} = (\tau^{\text{sigma, upper value of bin}}{}_{i,j} + \tau^{\text{sigma, lower value of bin}}{}_{i,j})/2 \, . \tag{6}$$

$\tau_{i,j}^{mean}$ is the mean cloud optical thickness associated with cell i at time j and is given by

$$\tau_{i,j}^{mean} = (\tau^{\text{mean, upper value of bin}}{}_{i,j} + \tau^{\text{mean, lower value of bin}}{}_{i,j})/2 \, . \tag{7}$$

Values for these parameters can be obtained from the D1 database (Table 1). The *erf(x)* function is defined as usual in terms of the normal (gaussian) distribution where

$$\frac{1}{\sigma\sqrt{2\pi}} \int_{-\infty}^{X} e^{\left(-\frac{1}{2}\right)\left(\frac{x - x_{mean}}{\sigma}\right)^2} dx \equiv \frac{1}{2}\left[1 + erf\left(\frac{1}{\sqrt{2}}\frac{X - x_{mean}}{\sigma}\right)\right] \; . \tag{8}$$

The integral expression on the left goes to 1 in the limit as X goes to infinity; σ is the standard deviation in Eq. (8). In Eq. (2) $\sum_{l=1}^{243} W_{i,j,l}$ is a normalization term which preserves the total area under the differential curve independent of the distribution function chosen for $W_{i,j,k}$.

Physically, the Q-matrix is interpreted to indicate the statistical fractional cloud coverage for a specific cell location, time, and cloud optical thickness (*i,j,k*).

3.2 Differential Fractional Cloud Coverage Distribution

The term $F_{region}(\tau_k) \cdot \Delta\tau_k$ is defined to be the time-averaged fractional coverage over the geographic *region* by clouds of optical thickness between τ_k and τ_{k-1} where $F_{region}(\tau_k)$ is given by

$$F_{region}(\tau_k) = \frac{1}{N}\sum_i\sum_j Q_{i,j,k} \tag{9}$$

and N is the number of *i,j* cells containing valid D1 data. The index values *i* selected for inclusion in the summation correspond to those cells contained within a particular geographic *region* (e.g. global sea, land, coastal, or defined geographic areas). The regions of interest chosen for this report are: global earth, global sea, global land, global coast, and the six 30°-latitude bands over sea, land, or coast with longitude $0° - 360°$. Since weather to a first approximation is cyclical, $F_{region}(\tau_k)$ is expected to become invariant with time as the number of years of data over which $F_{region}(\tau_k)$ is time-averaged increases. For the purposes of this report the index *j* extends over all daylight time periods within 1990 to 1993. Four years of data gives well-converged values of $F_{region}(\tau_k)$.

3.3 Integral Fractional Cloud Coverage Distribution

The integral distribution $I_{region}(\tau)$ of $F_{region}(\tau)$ given by

$$I_{region}(\tau) = \int_0^{\tau} F_{region}(\tau')d\tau' \tag{10}$$

is defined to be the time-averaged fractional coverage over the geographic *region* by clouds of optical thickness **less** than τ. Numerically, $I_{region}(\tau)$ has high resolution for small cloud optical thicknesses (e.g. see Figure 5). In the limit as τ goes to infinity, $I_{region}(\tau)$ goes to a value less than 1 corresponding to that fraction of the *region* covered by clouds of all optical thicknesses.

The integral distribution $J_{region}(\tau)$ of $F_{region}(\tau)$ given by

$$J_{region}(\tau) = \int_{\tau}^{\infty} F_{region}(\tau')d\tau' \tag{11}$$

is defined to be the time-averaged fractional coverage over the geographic *region* by clouds of optical thickness **greater** than τ. Numerically, $J_{region}(\tau)$ has high resolution for large cloud optical thicknesses (e.g. see Figure 6). In the limit as τ goes to zero, $J_{region}(\tau)$ goes to a value less than 1 corresponding to that fraction of the *region* covered by clouds of all optical thicknesses.

These methods in conjunction with D1 data can be used to define the cloud statistics for any geographic region and time period.

3.4 Effects of Variations in Cloud Optical Thickness within Cells

The difference in $F_{region}(\tau)$, $I_{region}(\tau)$, and $J_{region}(\tau)$ depending upon whether one assumes a uniform mean cloud optical thickness within each cell or a gaussian distribution in cloud optical thicknesses within each cell is now demonstrated. For the purposes of this comparison, we use D1 data for cloudy IR pixels (byte number 13) and the mean and sigma water paths (tau-values) for IR cloudy pixels (byte numbers 100 and 105, respectively). Evaluation of $F_{region}(\tau)$, $I_{region}(\tau)$, and $J_{region}(\tau)$ was done for global earth averaged over 4 years.

The results are shown in Figure 1, Figure 2, Figure 3, and Figure 20 and indicate that there is a significant difference in the cloud statistics depending upon whether one assumes a uniform optical cloud thickness within each cell (dotted line) or a gaussian distribution of cloud optical thicknesses (solid line) as specified by the standard deviation in tau for that respective cell. The statistical variation in cloud optical thickness enhances $F_{region}(\tau)$, $I_{region}(\tau)$, and $J_{region}(\tau)$ for tau values less than approximately 5 and greater than approximately 30. The enhancement increases with increasing tau so that at a tau value of 200, the enhancement is an order of magnitude as shown in Figure 3. Clearly, the statistical variation in cloud optical thicknesses within large cells can not be neglected for purposes of determining the probability of rare, optically thick (tau > 100) clouds.

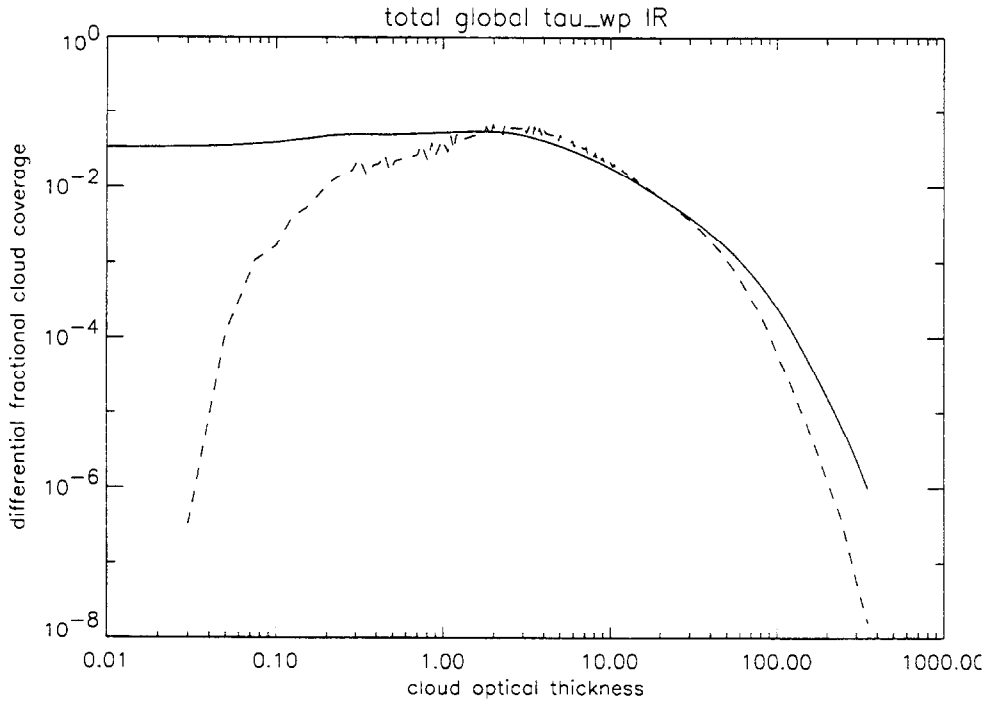

Figure 1 Total global time-averaged differential fractional cloud coverage versus cloud optical thickness (water path). The solid line assumes a gaussian distribution in tau values. The dotted line assumes a uniform cloud cover with zero standard deviation in tau.

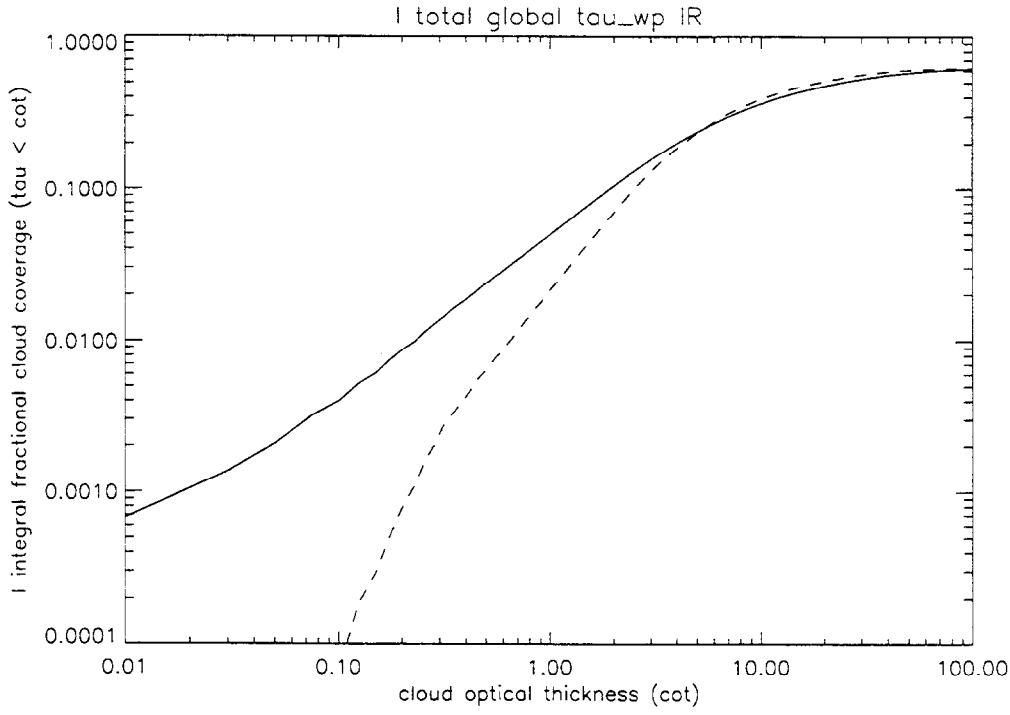

Figure 2 Total global time-averaged *I*-integral fractional cloud coverage versus cloud optical thickness (water path). The solid line assumes a gaussian distribution in tau values. The dotted line assumes a uniform cloud cover with zero standard deviation in tau.

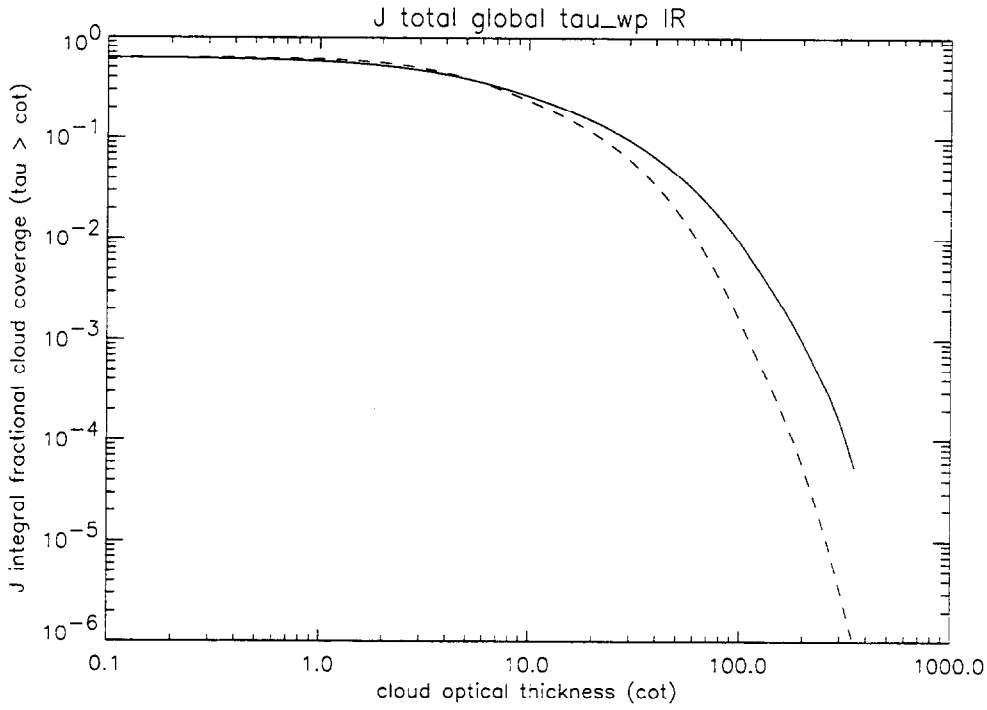

Figure 3 Total global time-averaged *J*-integral fractional cloud coverage versus cloud optical thickness (water path). The solid line assumes a gaussian distribution in tau values. The dotted line assumes a uniform cloud cover with zero standard deviation in tau.

4 Summary

The cloud coverage distributions for water path cloud optical thicknesses are presented graphically in Figure 4 through Figure 19 in Sec. 4.1. The same plots showing cloud coverage distributions versus albedo cloud optical thicknesses are presented in Figure 21 through Figure 36 in Sec. 4.2. All data in Figure 1 through Figure 36 have been time-averaged over the years 1990, 1991, 1992, and 1993. All of the plots in Figure 4 through Figure 18 and Figure 21 through Figure 35 include the effects of statistical variation in cloud optical thicknesses as determined by Eqs. (2) - (11) in Sec. 3.

In addition the time-averaged fractional cloud coverage is characterized in terms of various geographic regions. The regions chosen are: global earth, global sea, global land, global coast, and the six $30°$ -latitude bands over only sea, only land, and only coast with longitude $0° - 360°$. The cloud statistics over these geographic regions are characterized in terms of the time-averaged fractional cloud coverages $F_{region}(\tau_k)$, $I_{region}(\tau)$, and $J_{region}(\tau)$, which are defined in Secs. 3.2 and 3.3.

Plots of the differential cloud coverage in Figure 4 and Figure 21 show that the most probable cloud optical thickness on a global scale over sea, land or coast is approximately 2. In the case of the $J_{region}(\tau)$ -plots in Sec. 4.1 and 4.2, several arbitrary data points (*) denoted by the corresponding values of cloud optical thickness (COT), one-dimensional cloud transmission (CT) as determined from diffusion theory, and $J_{region}(\tau)$ (JI) are enumerated. Comparison of the numerical $J_{region}(\tau)$ values for cloud albedo data (Sec. 4.2) indicate that they are typically greater than the corresponding cloud water path data by factors of approximately 2; however, the overall trends for the two data sets are reasonably consistent.

Finally, we note that there is no significant statistical difference in the cloud optical thicknesses as specified by the mean tau for cloudy pixels (byte number 92) and mean tau for IR cloudy pixels (byte number 93) assuming uniform cloud cover (tau sigma defaulted to zero). This is demonstrated in Figure 19 and Figure 36.

This information (in conjunction with other information) is useful for assessing the statistical capabilities of satellite-based optical sensors with regard to imaging [12] and detecting optical signals beneath clouds [6].

4.1 Water Path Cloud Optical Thickness Distributions

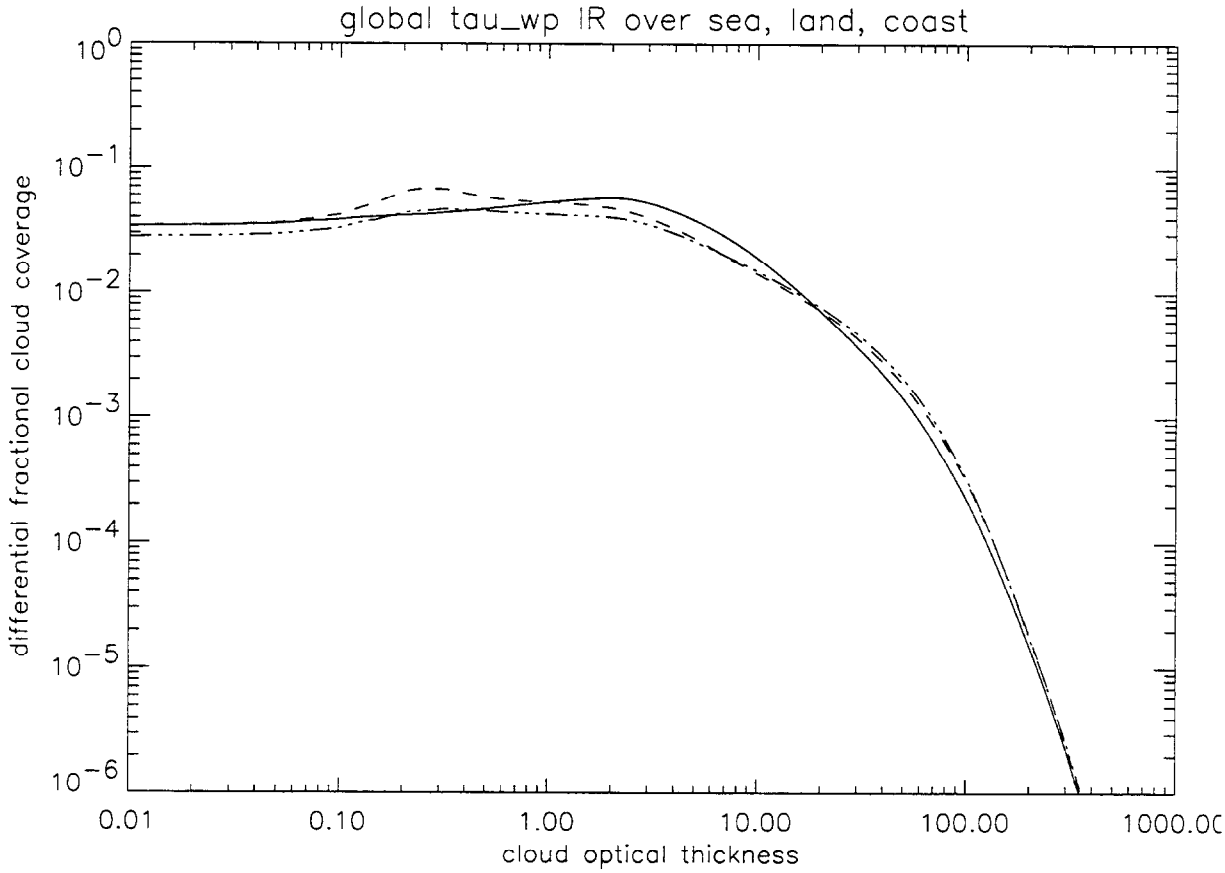

Figure 4 Global time-averaged differential fractional cloud coverage versus cloud optical thickness (water path) over sea (solid line), land (dashed), and coast (dash-dots).

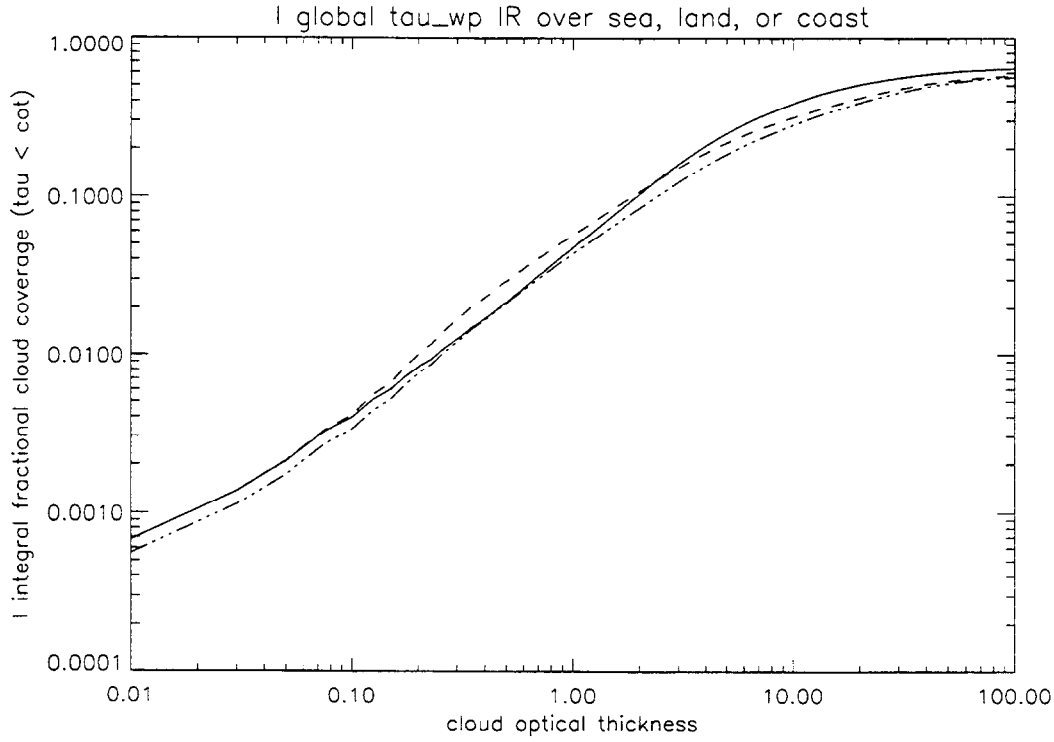

Figure 5 Global time-averaged *I*-integral fractional cloud coverage versus cloud optical thickness (water path) over sea (solid line), land (dashed), and coast (dash-dots).

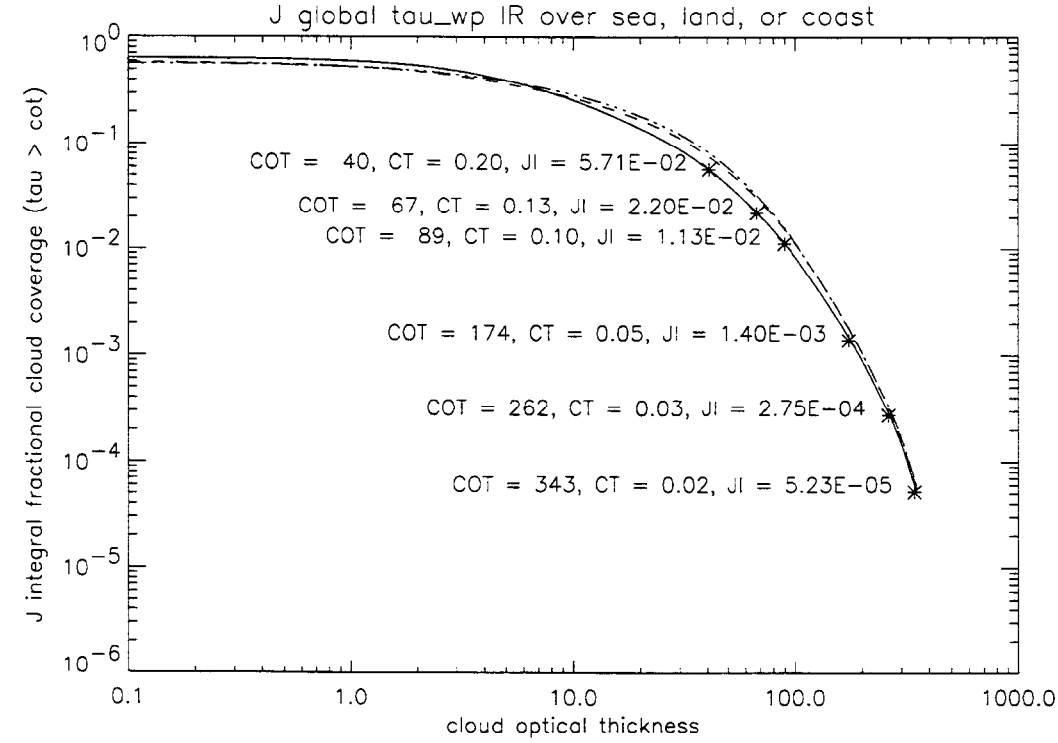

Figure 6 Global time-averaged *J*-integral fractional cloud coverage versus cloud optical thickness (water path) over sea (solid line), land (dashed), and coast (dash-dots).

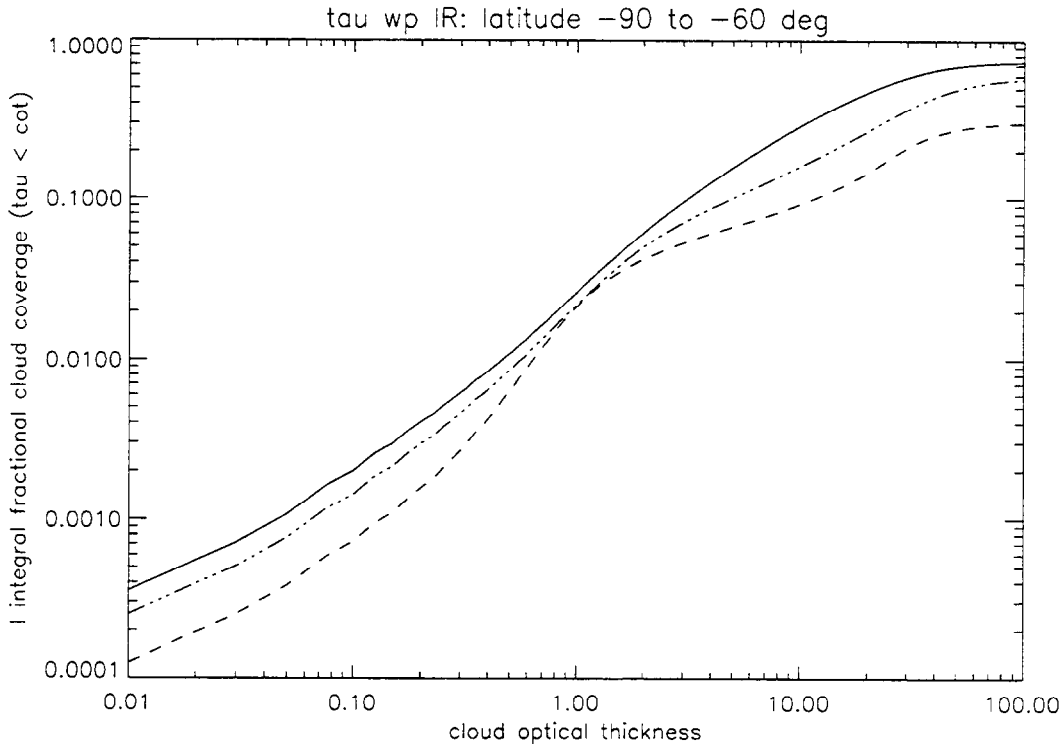

Figure 7 Time-averaged *I*-integral fractional cloud coverage for latitudes −90° to −60° versus cloud optical thickness (water path) over sea (solid line), land (dashed), and coast (dash-dots).

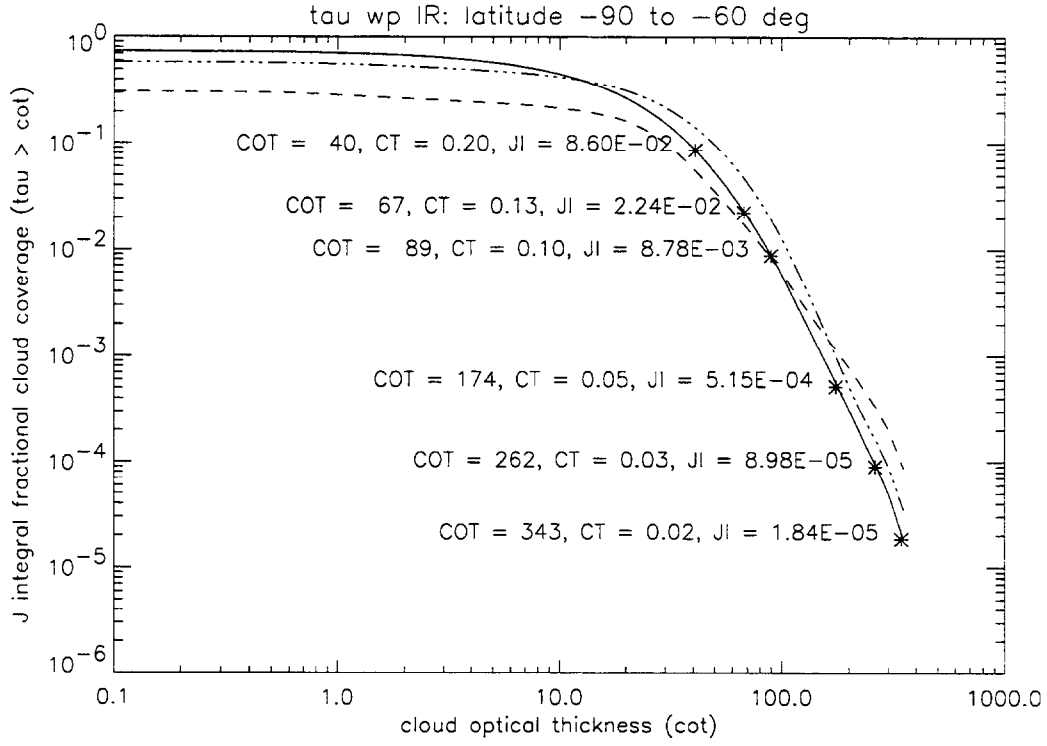

Figure 8 Time-averaged *J*-integral fractional cloud coverage for latitudes −90° to −60° versus cloud optical thickness (water path) over sea (solid line), land (dashed), and coast (dash-dots).

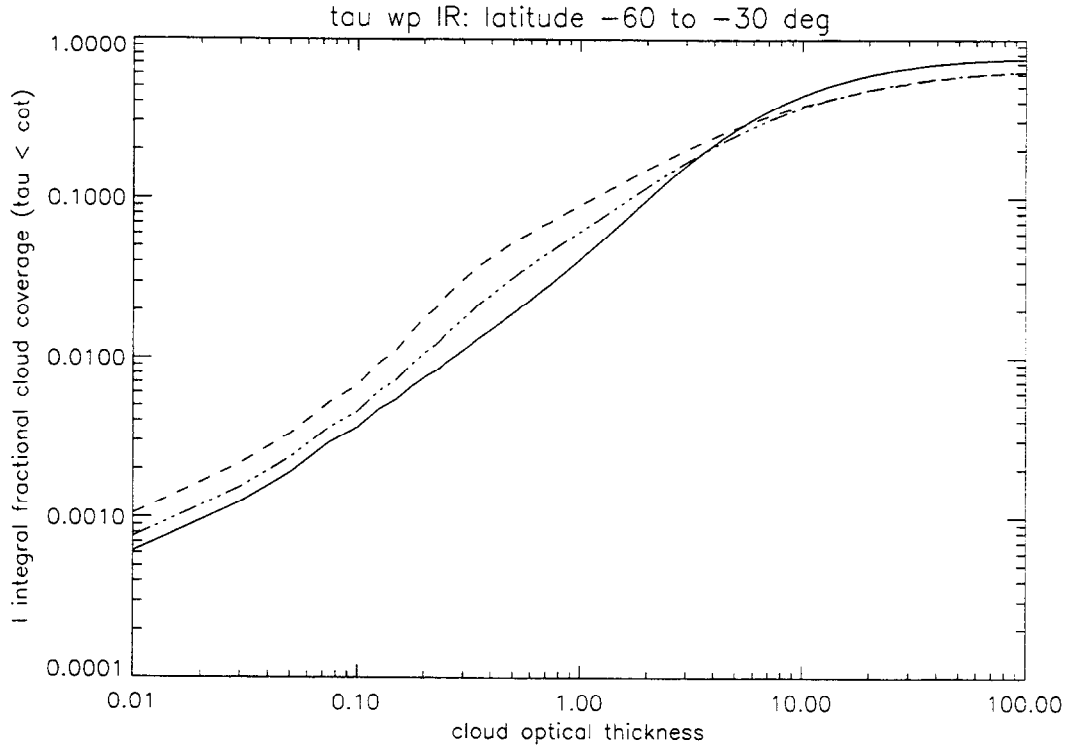

Figure 9 Time-averaged *I*-integral fractional cloud coverage for latitudes −60° to −30° versus cloud optical thickness (water path) over sea (solid line), land (dashed), and coast (dash-dots).

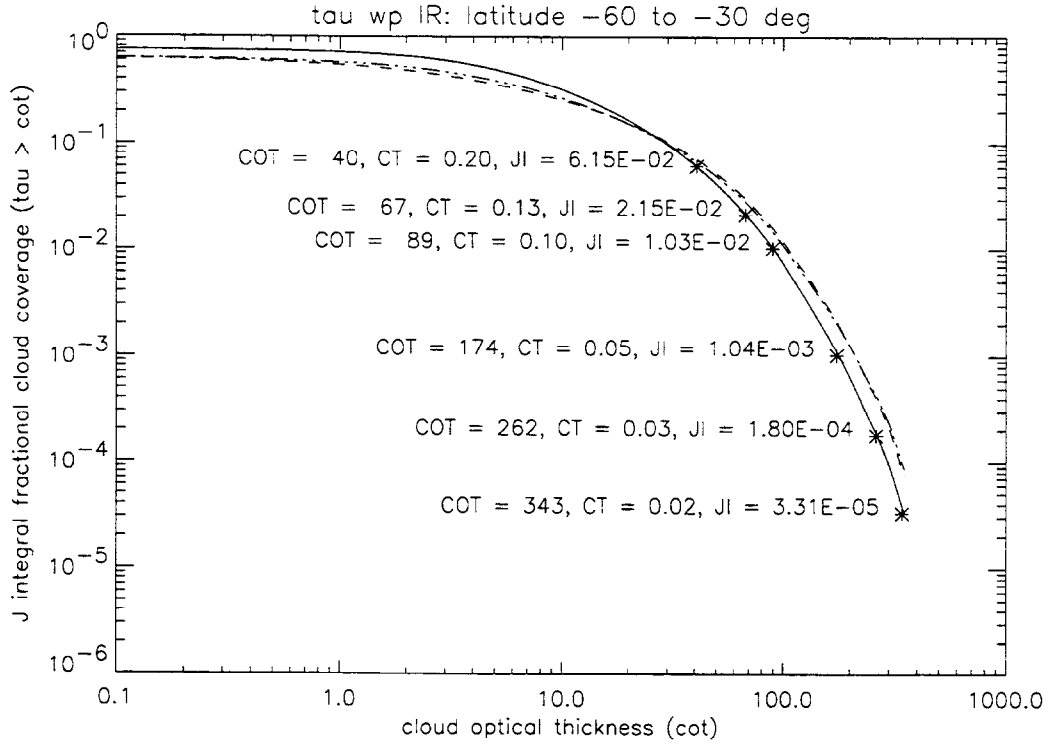

Figure 10 Time-averaged *J*-integral fractional cloud coverage for latitudes −60° to −30° versus cloud optical thickness (water path) over sea (solid line), land (dashed), and coast (dash-

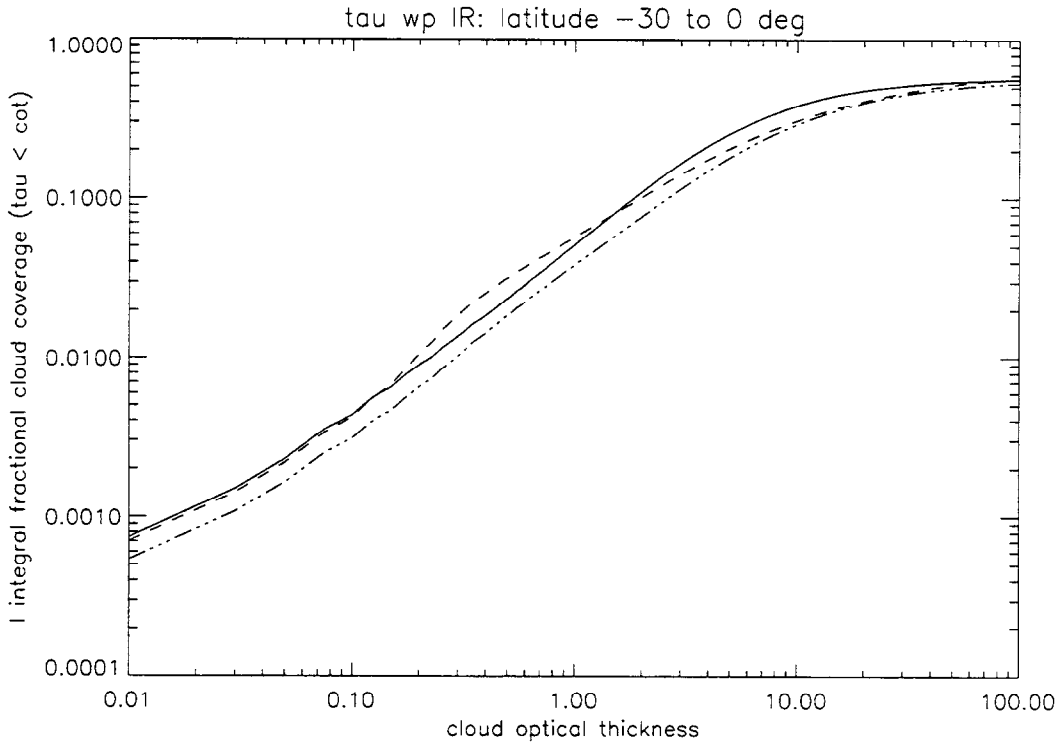

Figure 11 Time-averaged *I*-integral fractional cloud coverage for latitudes −30° to 0° versus cloud optical thickness (water path) over sea (solid line), land (dashed), and coast (dash-dots).

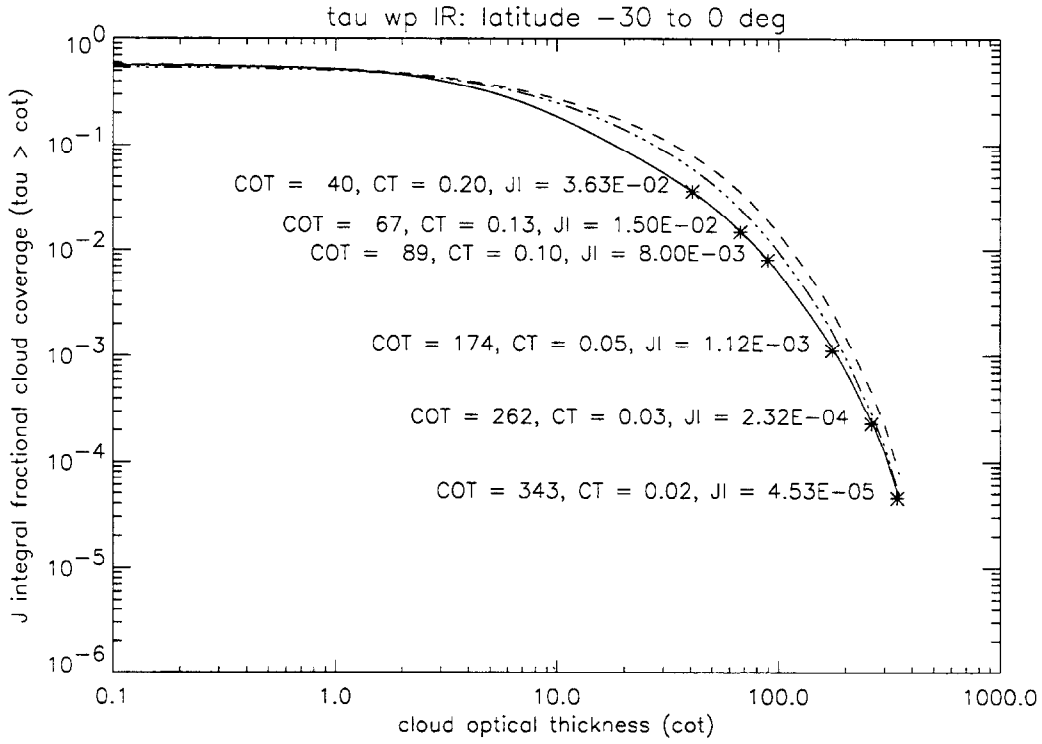

Figure 12 Time-averaged *J*-integral fractional cloud coverage for latitudes −30° to 0° versus cloud optical thickness (water path) over sea (solid line), land (dashed), and coast (dash-dots).

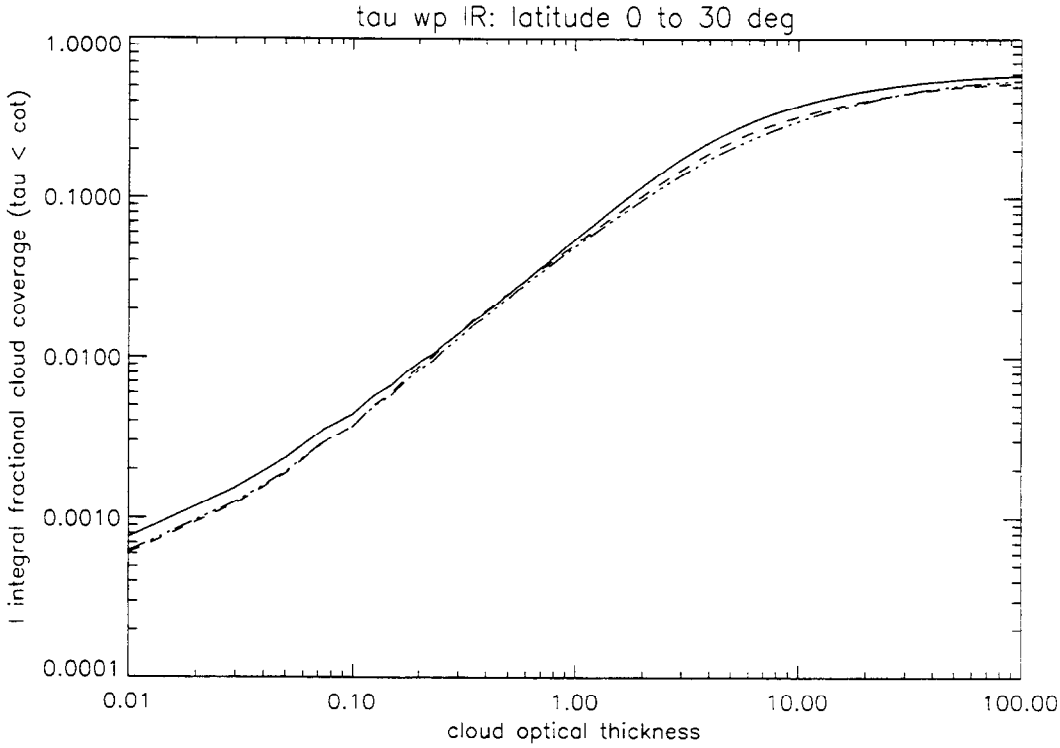

Figure 13 Time-averaged *I*-integral fractional cloud coverage for latitudes 0° to 30° versus cloud optical thickness (water path) over sea (solid line), land (dashed), and coast (dash-dots).

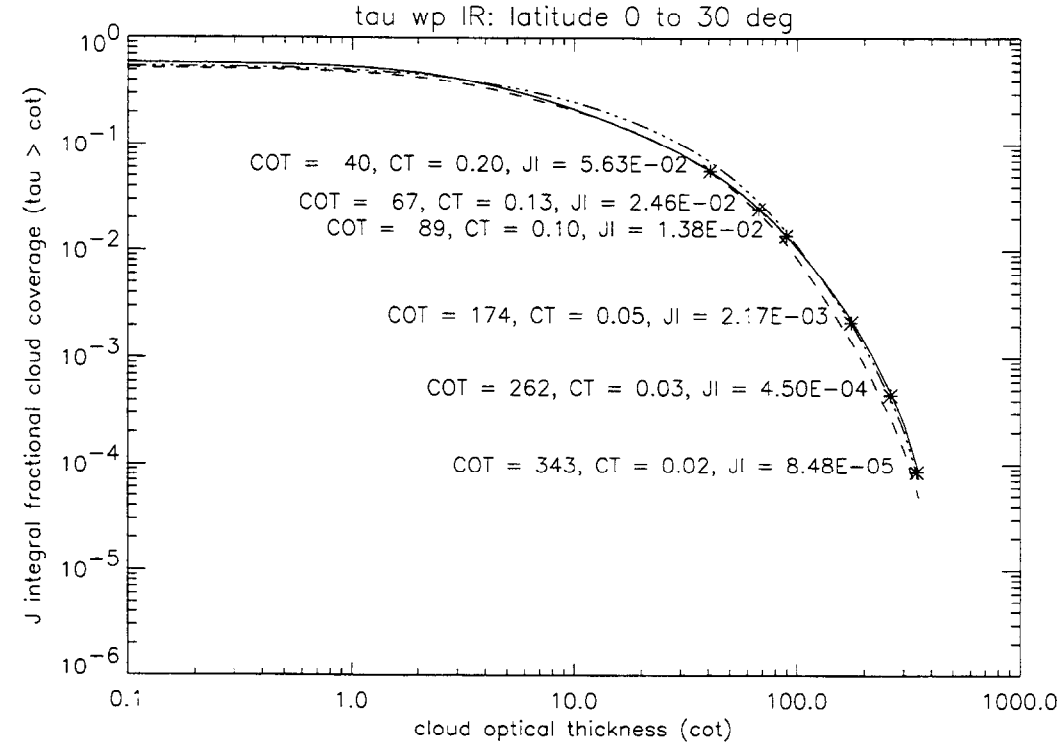

Figure 14 Time-averaged *J*-integral fractional cloud coverage for latitudes 0° to 30° versus cloud optical thickness (water path) over sea (solid line), land (dashed), and coast (dash-dots).

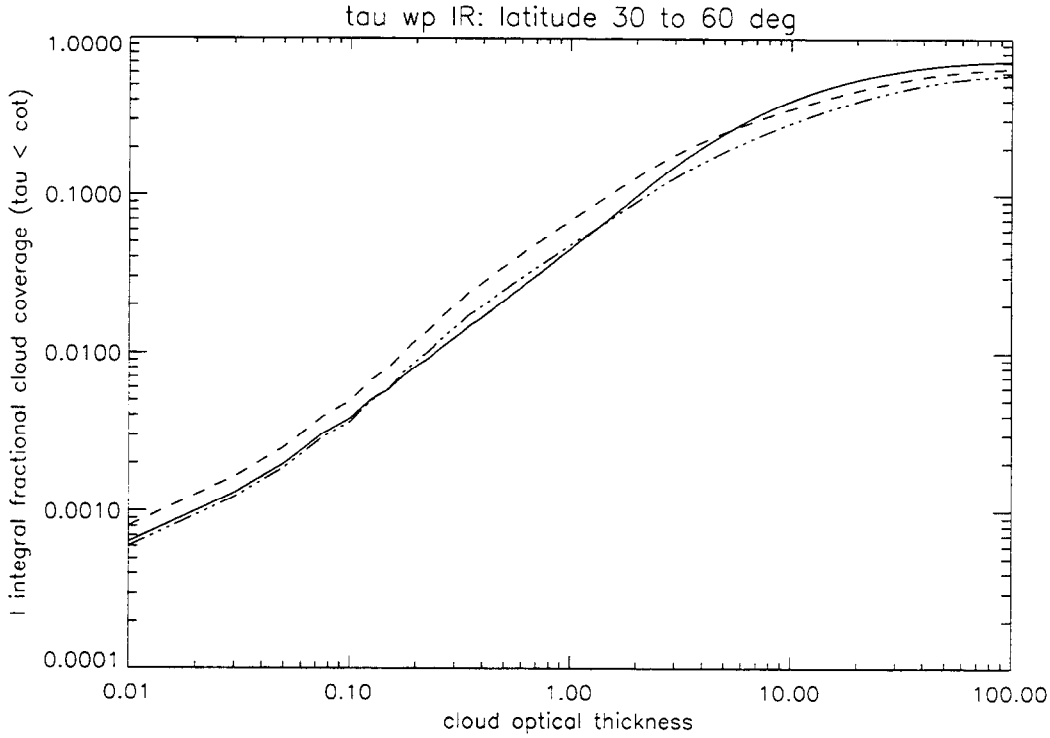

Figure 15 Time-averaged *I*-integral fractional cloud coverage for latitudes 30° to 60° versus cloud optical thickness (water path) over sea (solid line), land (dashed), and coast (dash-dots).

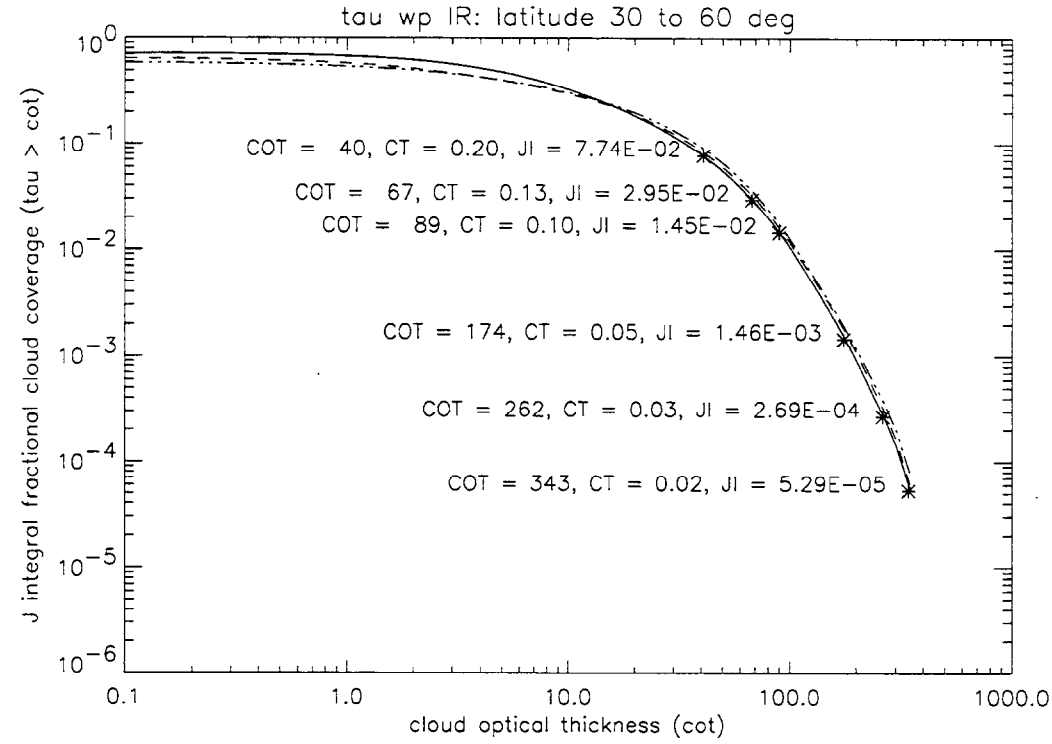

Figure 16 Time-averaged *J*-integral fractional cloud coverage for latitudes 30° to 60° versus cloud optical thickness (water path) over sea (solid line), land (dashed), and coast (dash-dots).

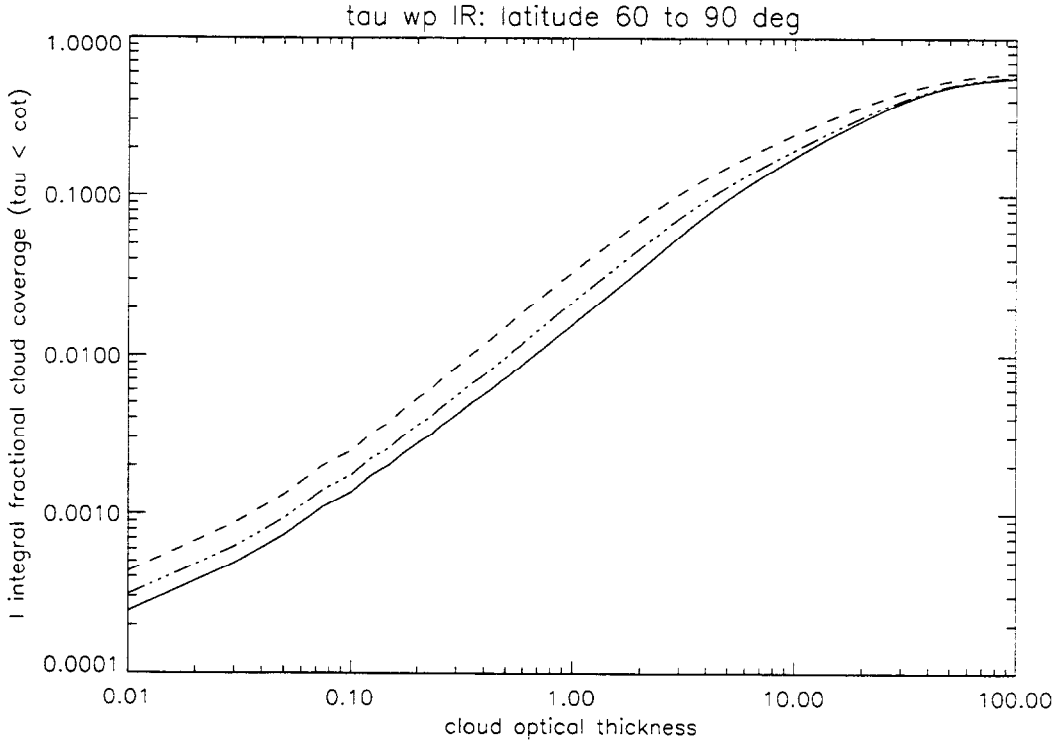

Figure 17 Time-averaged *I*-integral fractional cloud coverage for latitudes 60° to 90° versus cloud optical thickness (water path) over sea (solid line), land (dashed), and coast (dash-dots).

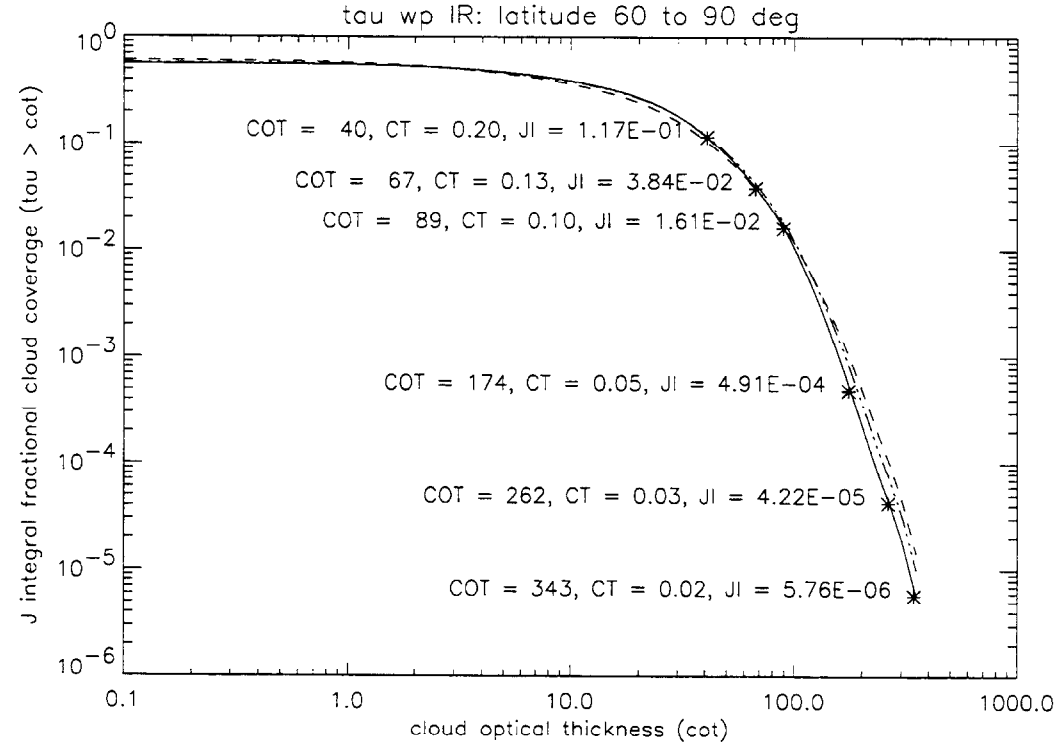

Figure 18 Time-averaged *J*-integral fractional cloud coverage for latitudes 60° to 90° versus cloud optical thickness (water path) over sea (solid line), land (dashed), and coast (dash-dots).

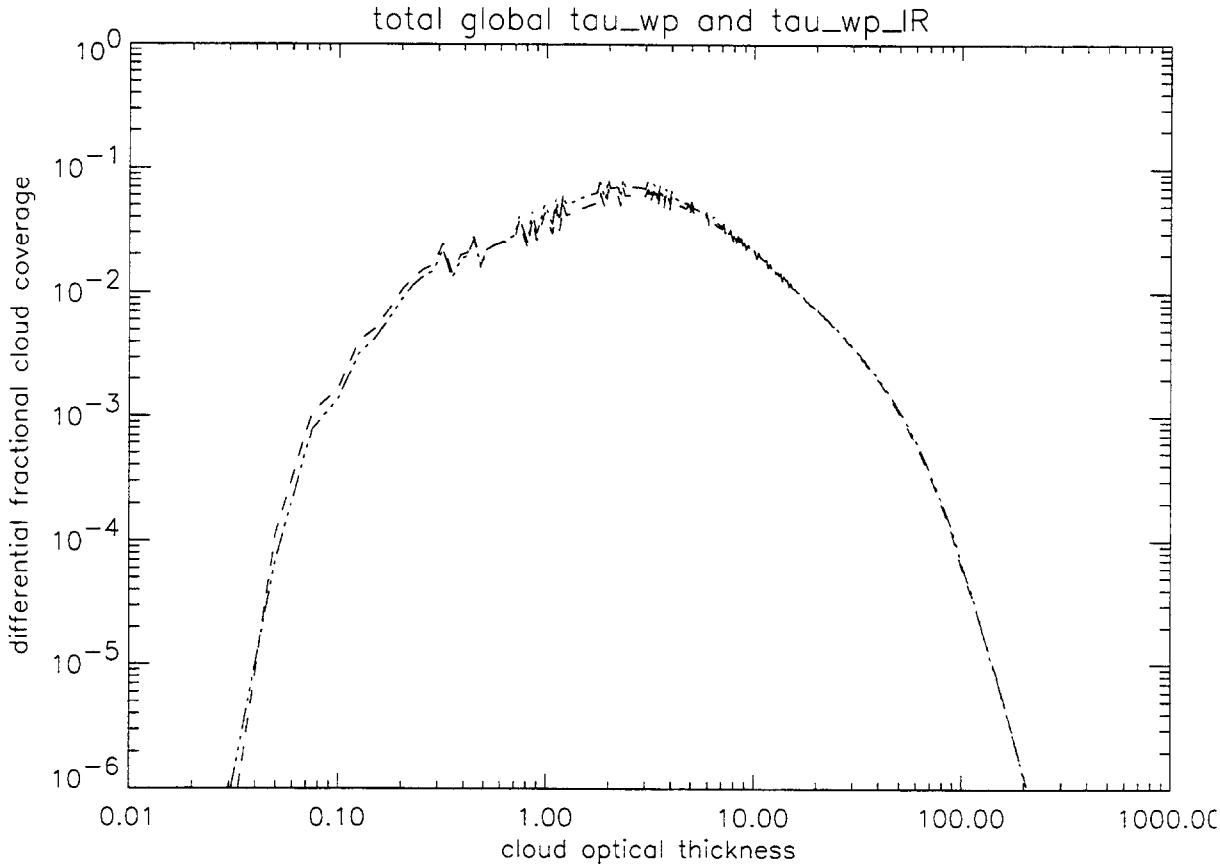

Figure 19 Total global time-averaged differential fractional cloud coverage versus cloud optical thickness (water path). The dashed line corresponds to the mean tau for IR cloudy pixels and the dash-dot-dot-dot line corresponds to the mean tau for cloudy pixels (Table 1). The origin of the systematic wiggles is discussed in Sec. 3.1.

4.2 Albedo Cloud Optical Thickness Distribution

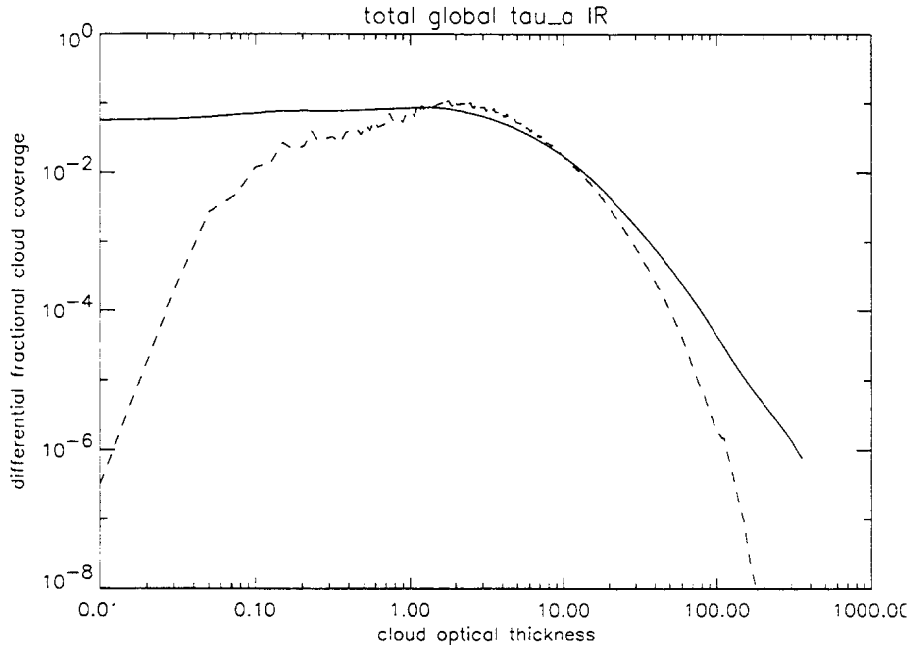

Figure 20 Total global time-averaged differential fractional cloud coverage versus cloud optical thickness (albedo). The solid line assumes a gaussian distribution in tau values. The dotted line assumes a uniform cloud cover with zero standard deviation in tau.

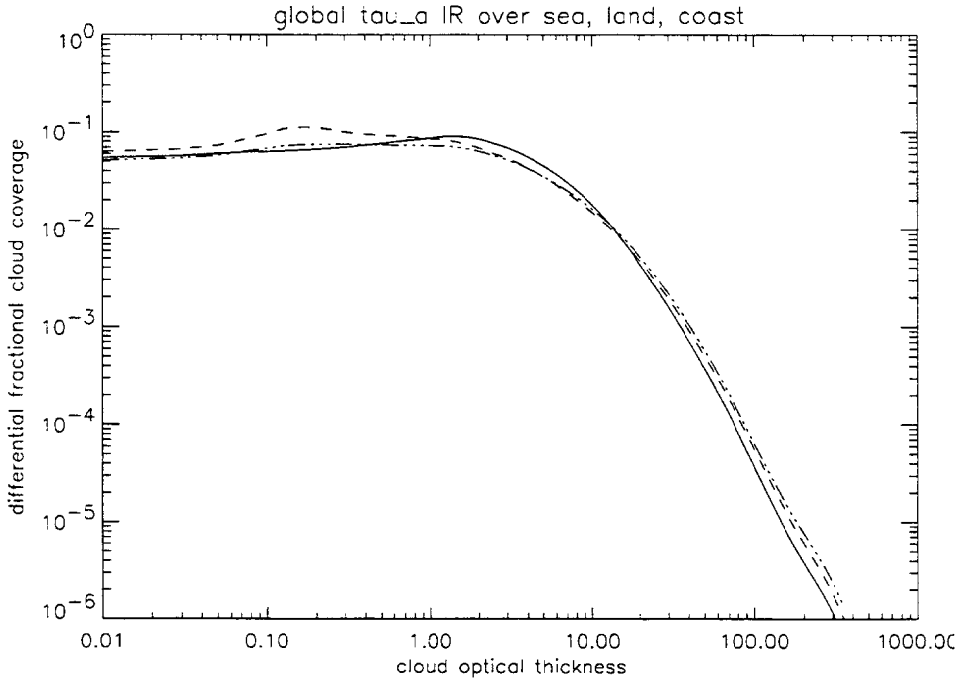

Figure 21 Global time-averaged differential fractional cloud coverage versus cloud optical thickness (water path) over sea (solid line), land (dashed), and coast (dash-dots).

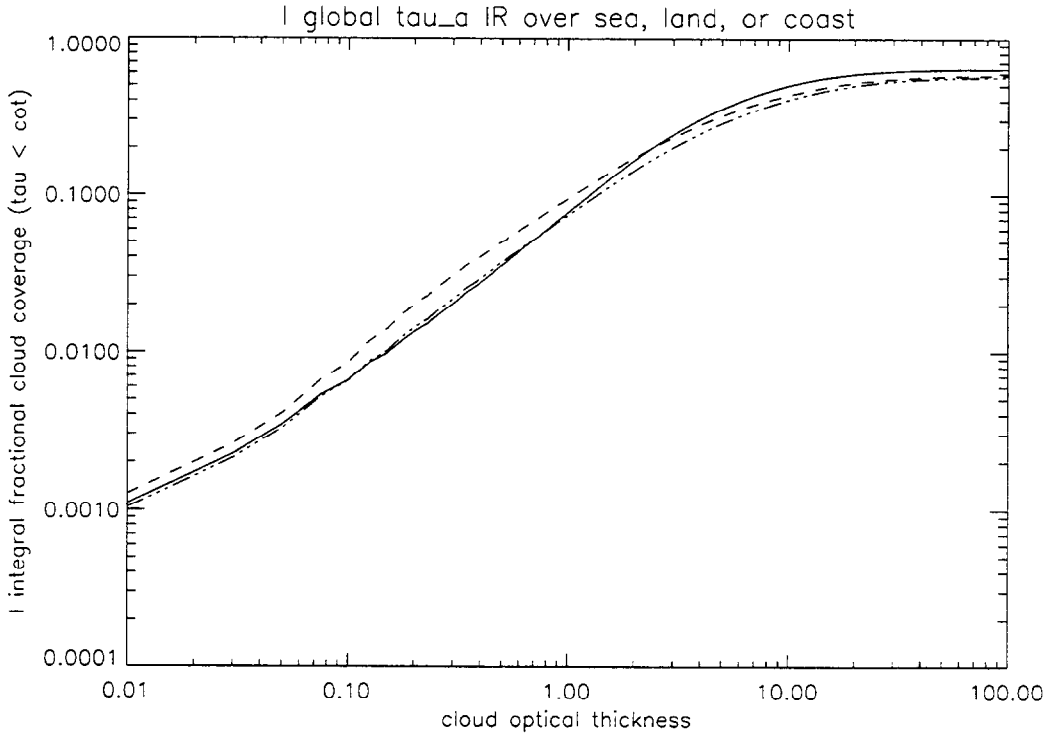

Figure 22 Global time-averaged *I*-integral fractional cloud coverage versus cloud optical thickness (albedo).

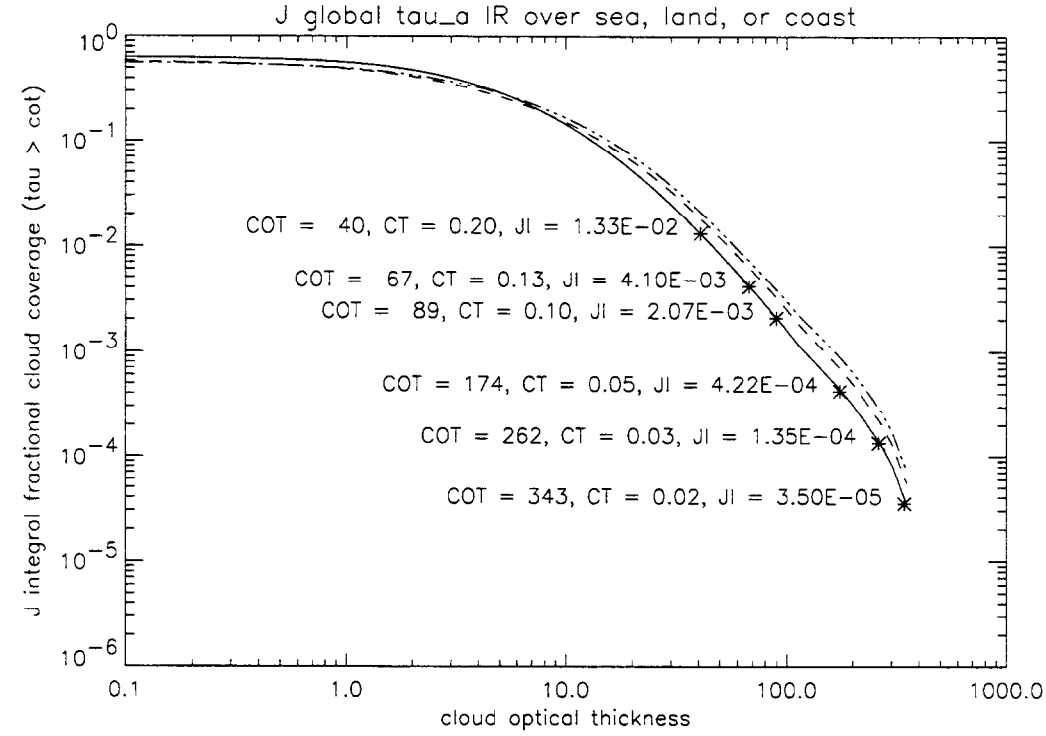

Figure 23 Global time-averaged *J*-integral fractional cloud coverage versus cloud optical thickness (albedo).

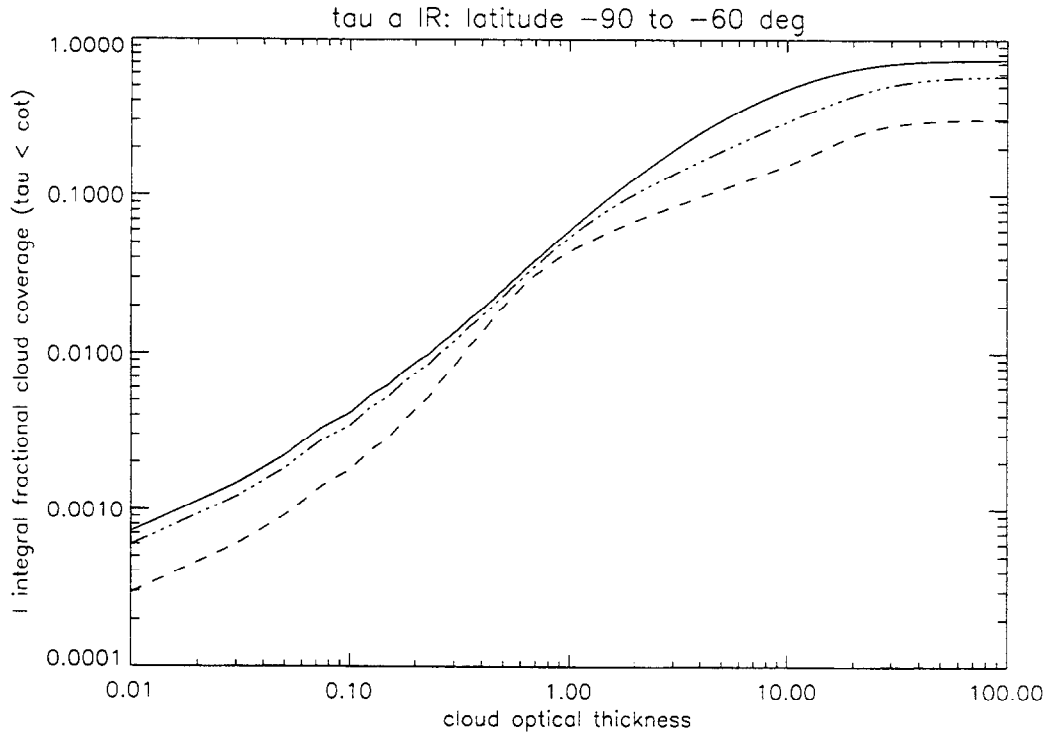

Figure 24 Time-averaged *I*-integral fractional cloud coverage for latitudes −90° to −60° versus cloud optical thickness (albedo) over sea (solid line), land (dashed), and coast (dash-dots).

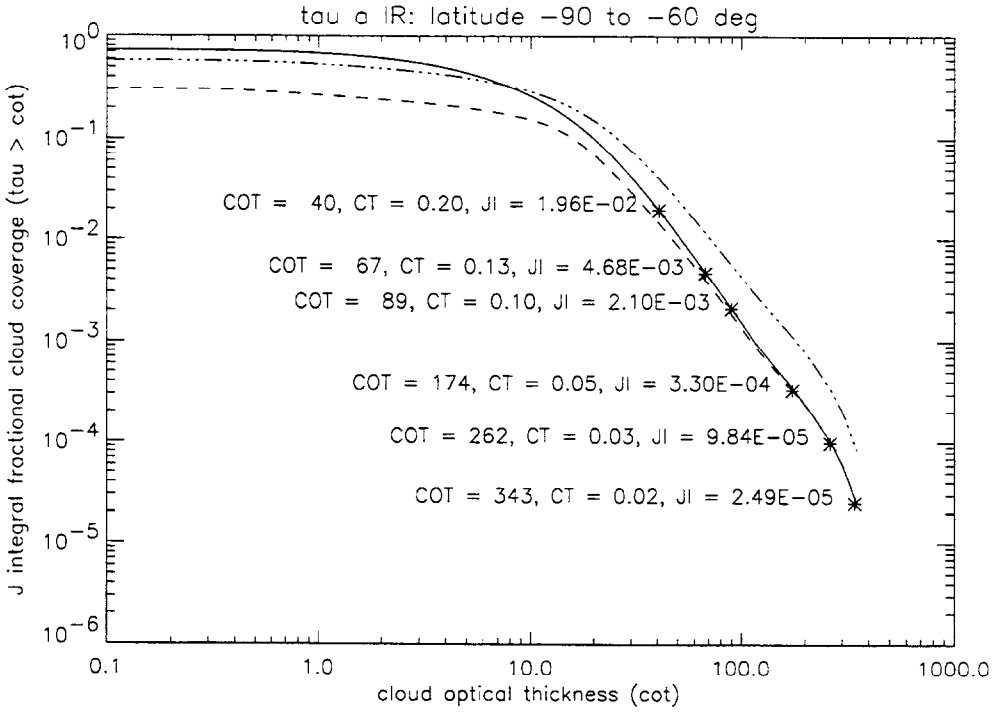

Figure 25 Time-averaged *J*-integral fractional cloud coverage for latitudes −90° to −60° versus cloud optical thickness (albedo) over sea (solid line), land (dashed), and coast (dash-dots).

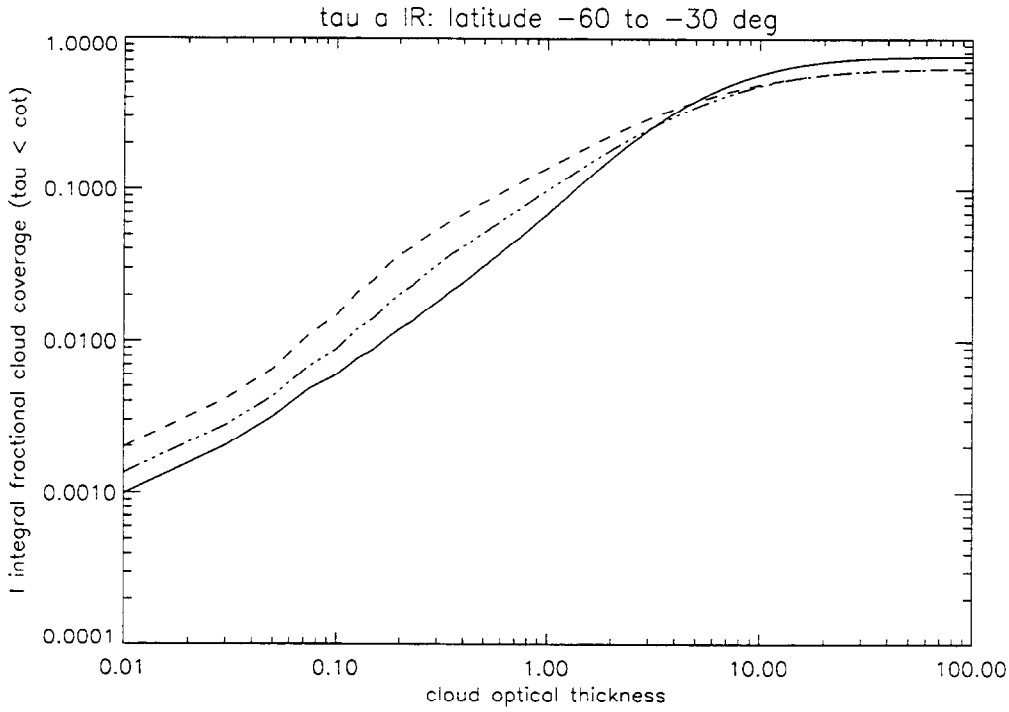

Figure 26 Time-averaged *I*-integral fractional cloud coverage for latitudes −60° to −30° versus cloud optical thickness (albedo) over sea (solid line), land (dashed), and coast (dash-dots).

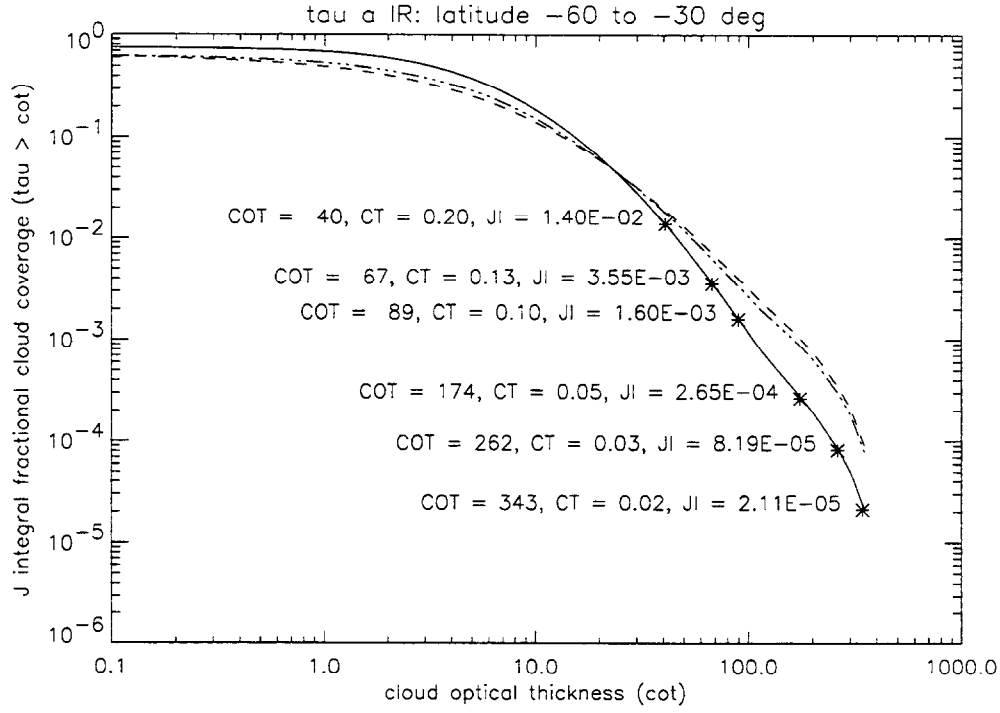

Figure 27 Time-averaged *J*-integral fractional cloud coverage for latitudes −60° to −30° versus cloud optical thickness (water path) over sea (solid line), land (dashed), and coast (dash-dots).

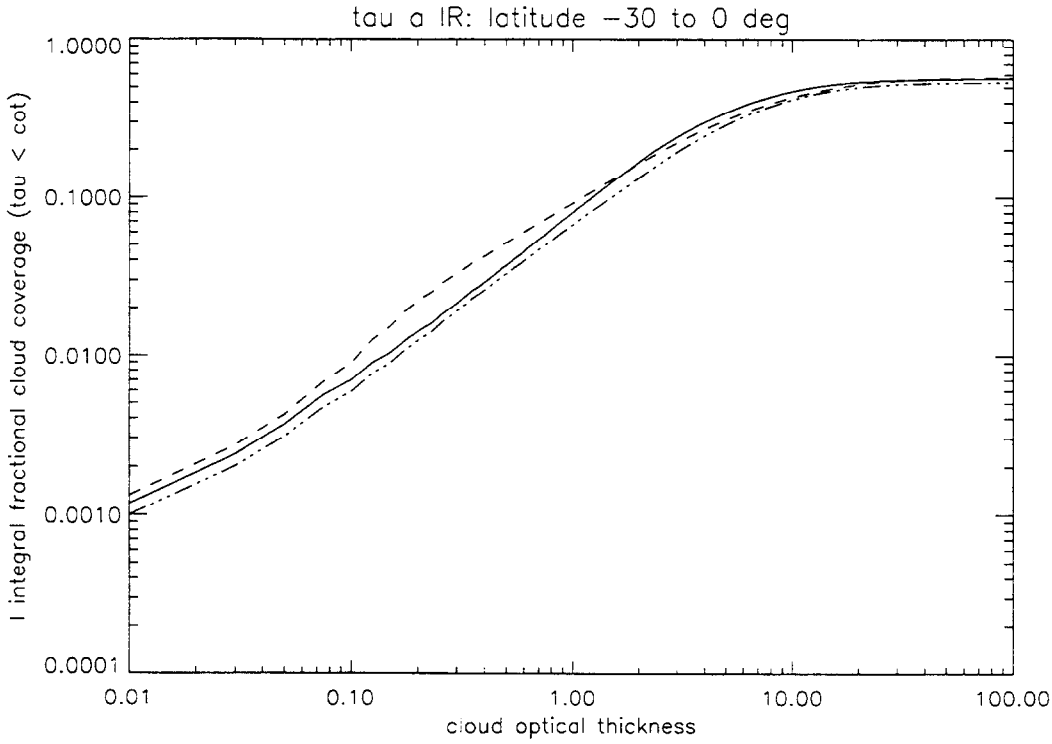

Figure 28 Time-averaged *I*-integral fractional cloud coverage for latitudes −30° to 0° versus cloud optical thickness (water path) over sea (solid line), land (dashed), and coast (dash-dots).

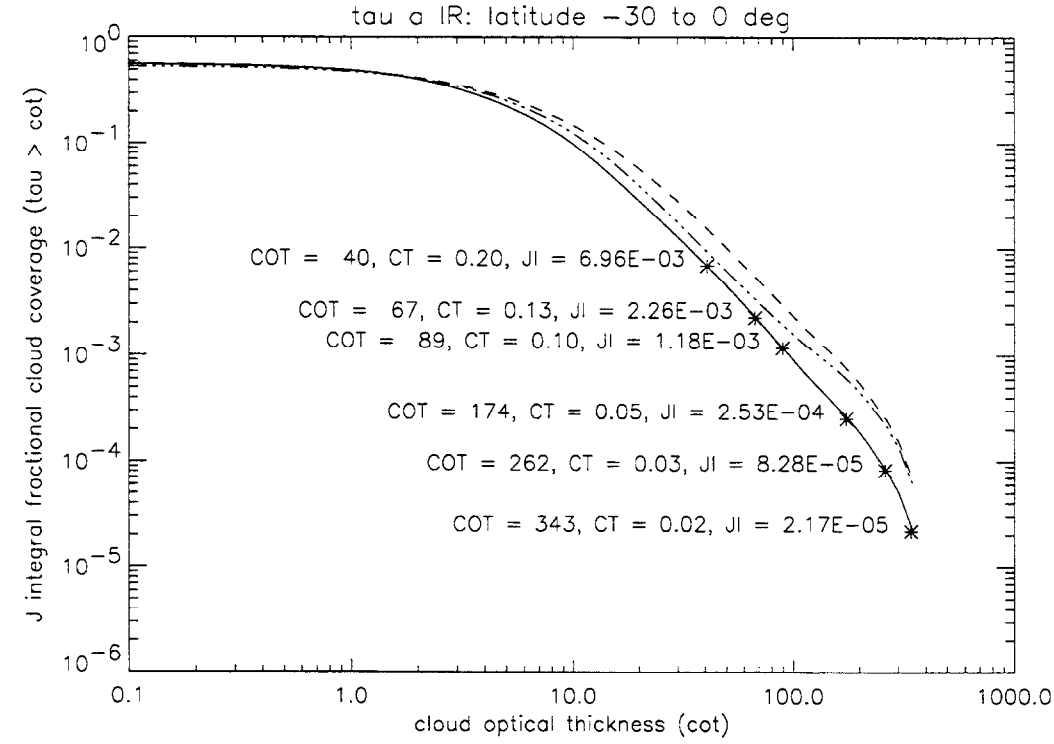

Figure 29 Time-averaged *J*-integral fractional cloud coverage for latitudes −30° to 0° versus cloud optical thickness (water path) over sea (solid line), land (dashed), and coast (dash-dots).

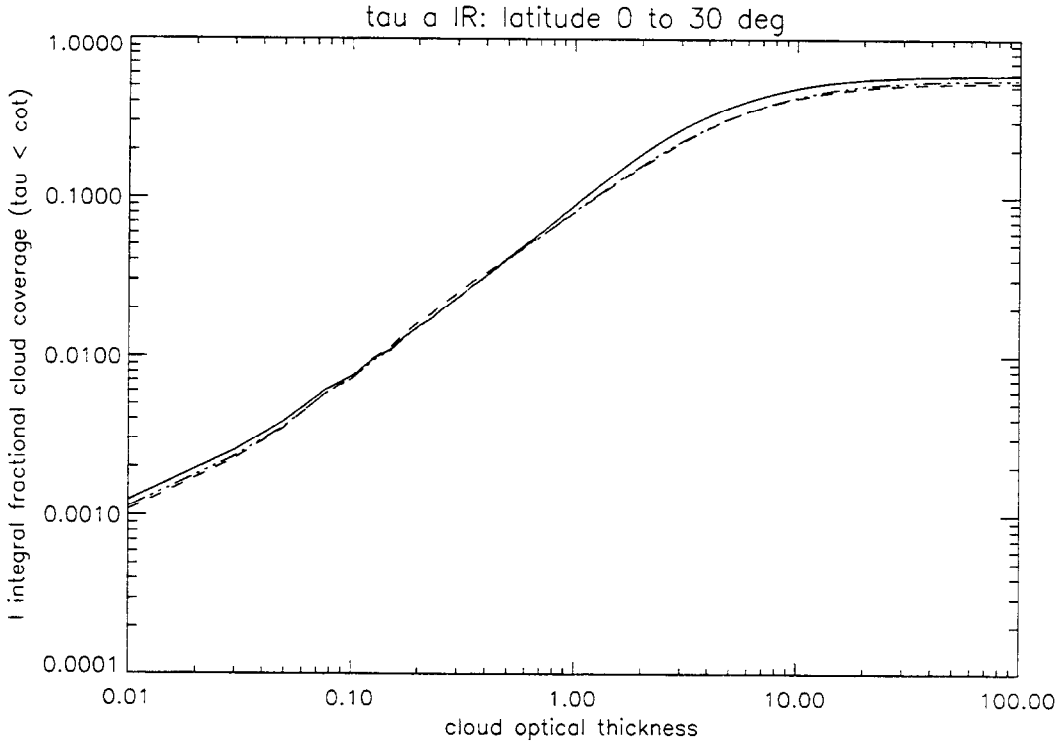

Figure 30 Time-averaged *I*-integral fractional cloud coverage for latitudes 0° to 30° versus cloud optical thickness (water path) over sea (solid line), land (dashed), and coast (dash-dots).

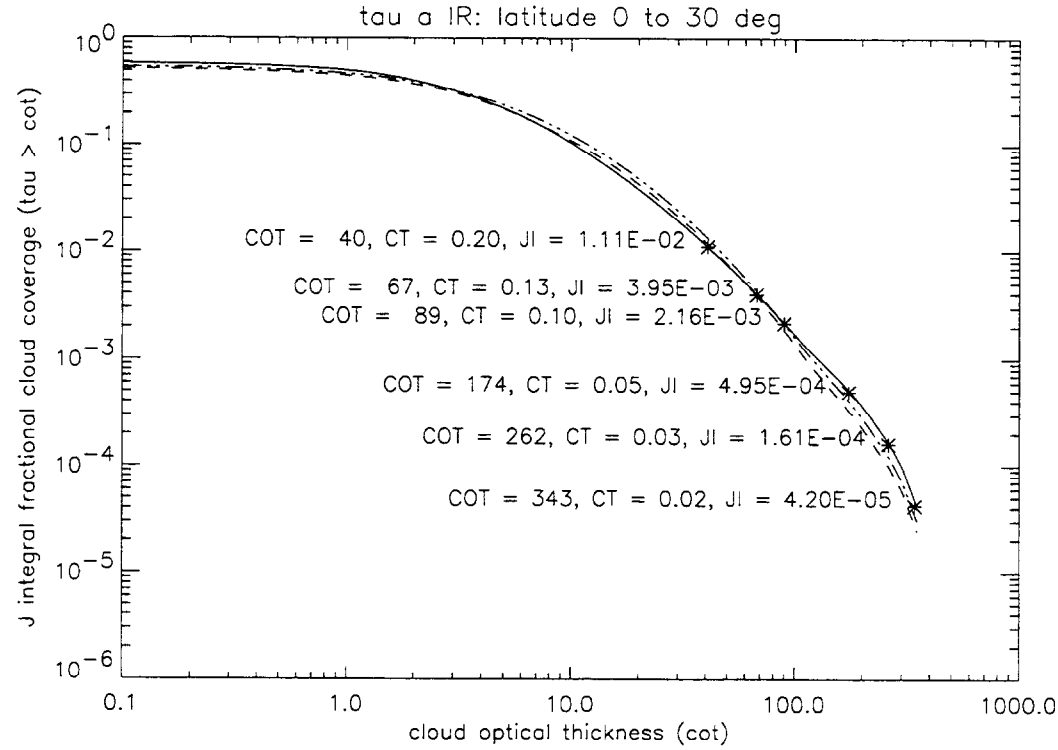

Figure 31 Time-averaged *J*-integral fractional cloud coverage for latitudes 0° to 30° versus cloud optical thickness (water path) over sea (solid line), land (dashed), and coast (dash-dots).

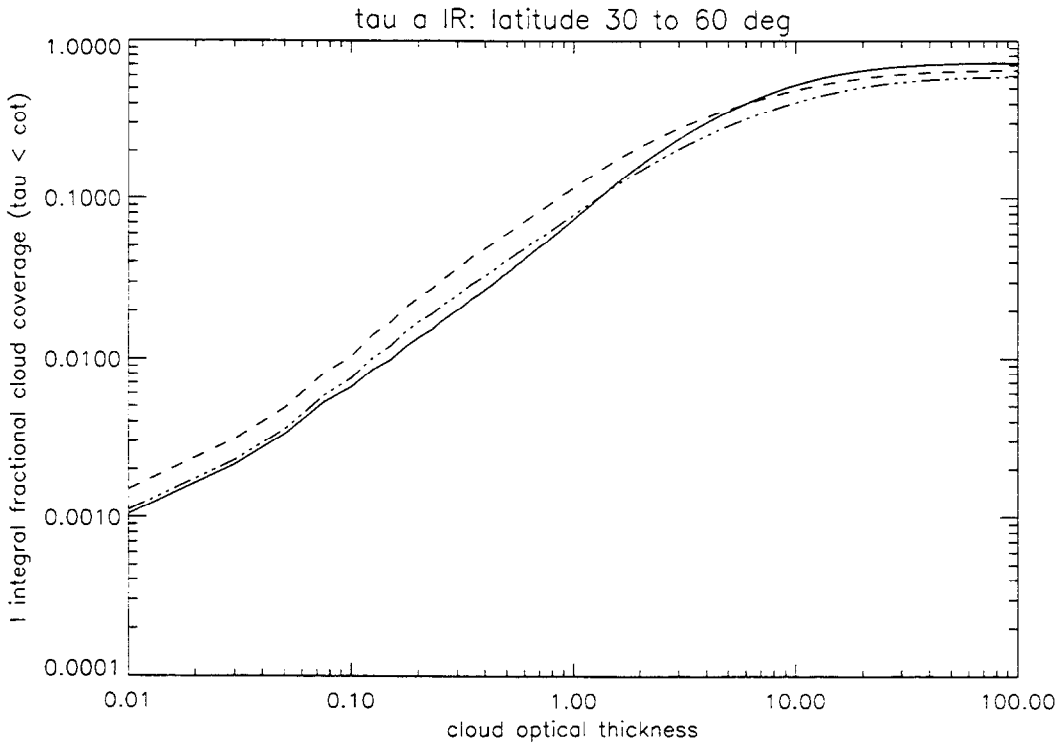

Figure 32 Time-averaged *I*-integral fractional cloud coverage for latitudes 30° to 60° versus cloud optical thickness (water path) over sea (solid line), land (dashed), and coast (dash-dots).

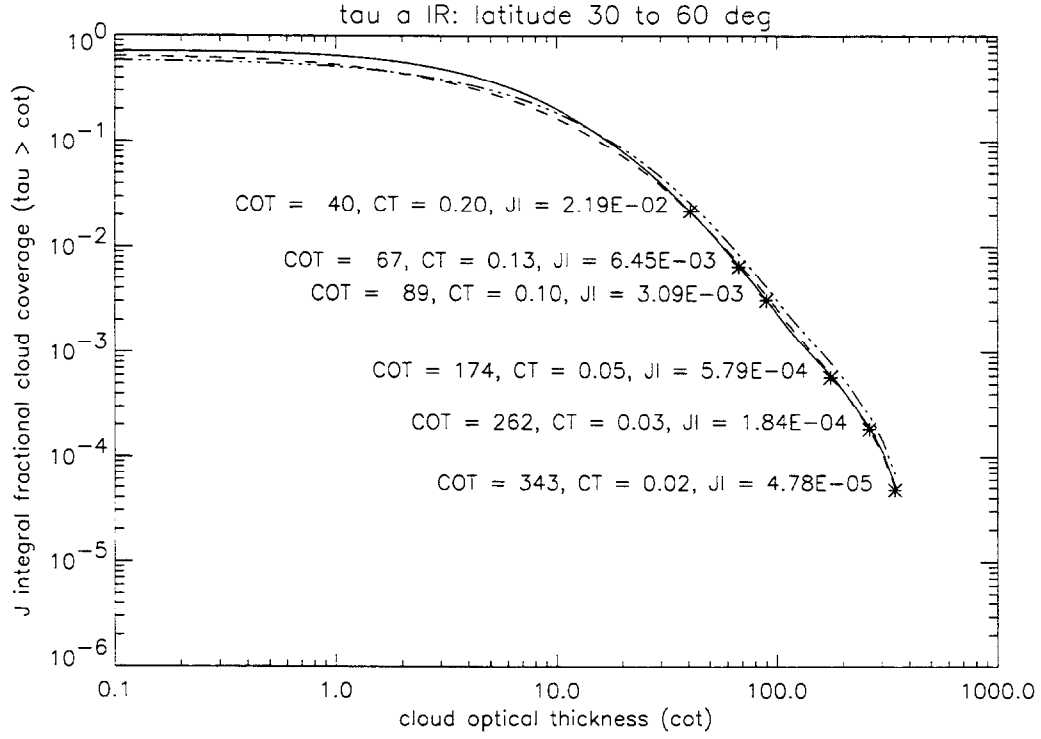

Figure 33 Time-averaged *J*-integral fractional cloud coverage for latitudes 30° to 60° versus cloud optical thickness (water path) over sea (solid line), land (dashed), and coast (dash-dots).

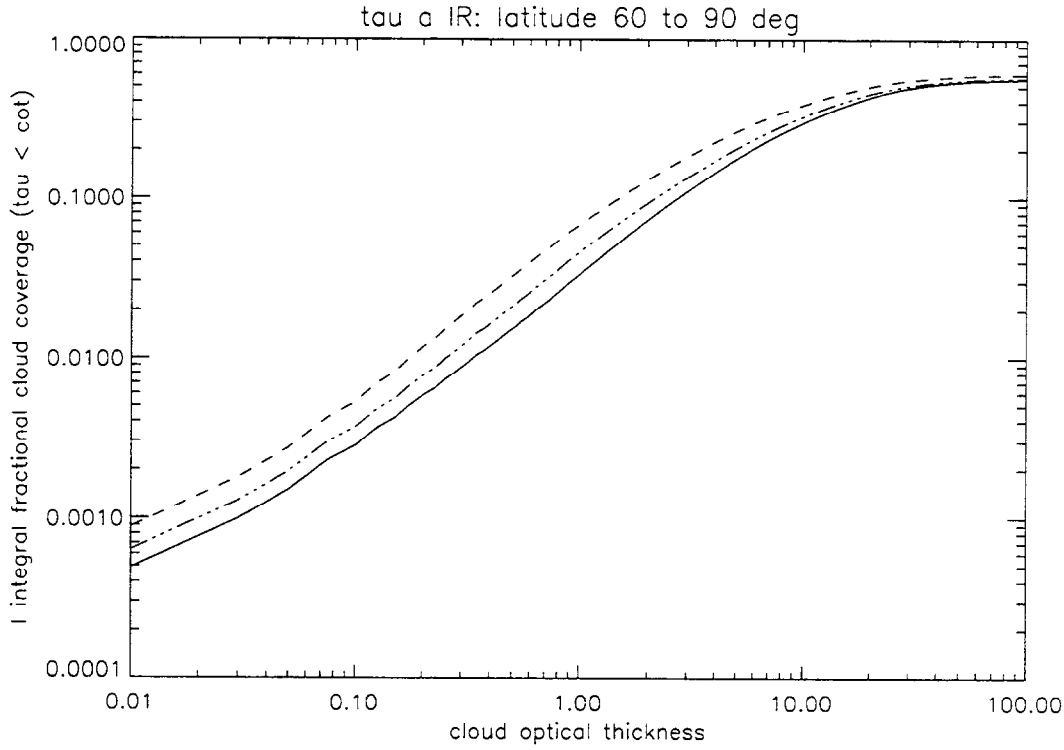

Figure 34 Time-averaged *I*-integral fractional cloud coverage for latitudes 60° to 90° versus cloud optical thickness (water path) over sea (solid line), land (dashed), and coast (dash-dots).

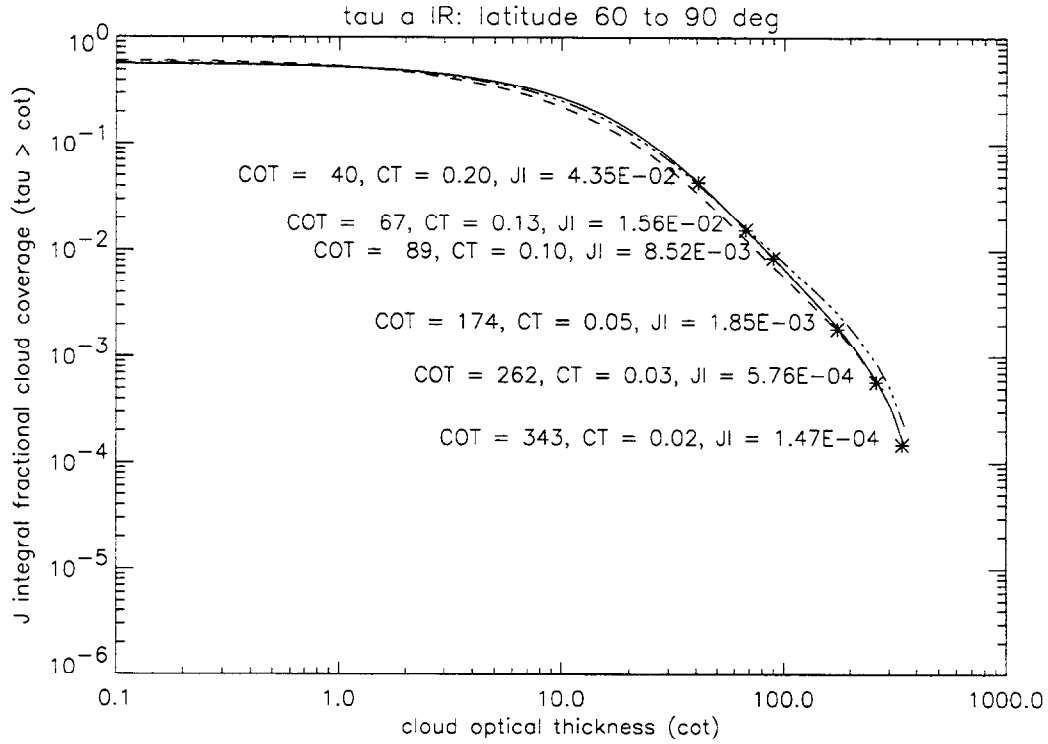

Figure 35 Time-averaged *I*-integral fractional cloud coverage for latitudes 60° to 90° versus cloud optical thickness (water path) over sea (solid line), land (dashed), and coast (dash-dots).

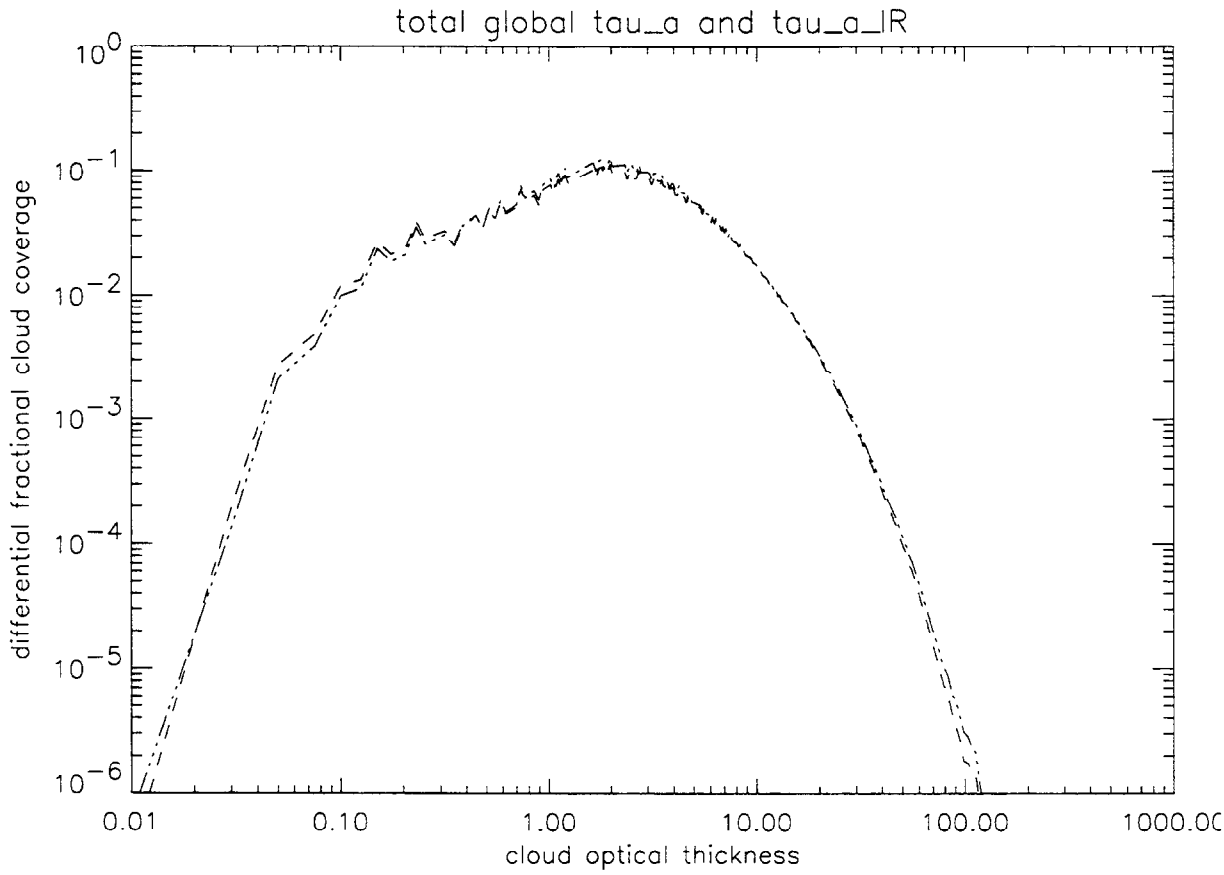

Figure 36 Total global time-averaged differential fractional cloud coverage versus cloud optical thickness (albedo). The dashed line corresponds to the mean tau for IR cloudy pixels and the dash-dot-dot-dot line corresponds to the mean tau for cloudy pixels (Table 1). The origin of the systematic wiggles is discussed in Sec. 3.1.

5 References

1 W. B. Rossow and R. A. Schiffer, "ISCCP Cloud Data Products", Bulletin of the American Meteorological Society, **72**, 1 (1991).

2 W. B. Rossow, A. Walker, and M. Roiter, "International Satellite Cloud Climatology Project (ISCCP) Description of Reduced Resolution Radiance Data", http://isccp.giss.nasa.gov/

3 G. Seze and W. B. Rossow, "Time-cumulated visible and infrared radiance histograms used as descriptors of surface and cloud variations", Int J. Remote Sensing, **12**, 877-920, 1991.

4 G. Seze and W. B. Rossow, "Effects of satellite data resolution on measuring the space-time variations of surfaces and clouds", Int. J. Remote Sensing, **12**, 921-952, 1991.

5 W. B. Rossow, A. W. Walker, D. E. Beuschel, and M. D. Roiter, "International Satellite Cloud Climatology Project: Documentation of New Cloud Datasets", http://isccp.giss.nasa.gov/

6 K. L. Brower, "Optical Transmission of Light through Clouds", Sandia National Laboratories, Albuquerque, New Mexico, 87185-0977, Report SAND97-1139, May 1997.

7 S. G. Warren, "Optical constants of ice from the ultraviolet to the microwave", *Applied Optics*, **23** (8), 1206 (1984).

8 E. Whalley, *J. Phys. Chem.* **87**, 4174 (1983).

9 H. C. van de Hulst, *Light Scattering by Small Particles*, (Dover Publications, New York, 1981).

10 Stephen Gentry, Sandia National Laboratories, private communication, May, 1998.

11 Raymond Ostensen, Sandia National Laboratories, private communication, May, 1998.

12 K. L. Brower, "Apparent Spatial Blurring and Displacement of a Point Optical Source due to Cloud Scattering", Sandia National Laboratories, Albuquerque, New Mexico, 87185-0977, Report SAND97-2164, September 1997.

THIS PAGE LEFT INTENTIONALLY BLANK.

Distribution

1 S. Craig Fox
1227 S. Patrick Drive
Ste 110
Satellite Beach, FL 32937

1 Maj. Bill Hilbun
HQ AFTAC/TTA
1030 S. Highway A1A
Patrick AFB, FL 32935-3002

1 Capt. Jon Hodge
HQ AFTAC/TTA
1030 S. Highway A1A
Patrick AFB, FL 32935-3002

1 Lt. Col. Debra Matson
SMC/CZZ
2435 Vela Way
Suite 1613
LAAFB, El Segundo, CA 90245-5500

1 Joe Marshall
HQ AFTAC/TTA
1030 S. Highway A1A
Patrick AFB, FL 32935-3002

1 Darren Sene
NAIC/DXDI
4180 Watson Way
Wright-Patterson AFB, OH 45433

Lawrence Livermore National Laboratory
1 Hans Kruger, LLL/MS L-173
1 D. Lynn Shaeffer, LLL/MS L-84

Los Alamos National Laboratory
1 Mark Hodgson, LANL/NIS-RD
1 Eugene Symbalisty, LANL/EES-8, F659

Sandia National Laboratories
1 MS 0987 Richard Wickstrom, 2611
1 MS 0425 Michael Edenburn, 5415
1 MS 0970 James Kelsey, 5700
1 MS 0971 Gary Mauth, 5703

1	MS 0972	Clinton Boye, 5705
3	MS 0967	Norman Blocker, 5706
3	MS 0967	Sandra Spraggins, 5706
1	MS 0973	John Williams, 5707
1	MS 0973	Stephanie Eras, 5707
1	MS 0973	Walter Huebner, 5707
1	MS 0973	Don Rountree, 5707
1	MS 0965	Kurt Lanes, 5711
1	MS 0972	Anthony Medina, 5722
1	MS 0972	Timothy Bates, 5722
1	MS 0972	Gregory Christiansen, 5722
2	MS 0972	Dean Dixon, 5722
1	MS 0972	John Falls, 5722
1	MS0980	Philip Green, 5725
1	MS 0980	Stephen Gentry, 5725
1	MS 0980	Carter Grobeck, 5725
1	MS 0980	Karen Jefferson, 5725
1	MS 0980	Lubomyra Kmetyk, 5725
1	MS 0980	Ron Schmidt, 5725
1	MS 0980	John Taylor, 5725
1	MS 0980	Charles Vittitoe, 5725
1	MS 0978	Richard Spalding, 5909
1	MS 1140	James Rice, 6500
1	MS 0977	William Cook, 6524
30	MS 0977	Department 6524 Algorithm File, 6524
1	MS 1138	John Rowe, 6531
1	MS 1138	Bill Richard, 6533
1	MS 9018	Central Technical Files, 8940-2
2	MS 0899	Technical Library, 4916
2	MS 0619	Review & Approval Desk, 12690 For DOE/OSTI